

1   **DNA repair and anti-cancer mechanisms in the longest-living mammal: the**  
2   **bowhead whale**

3

4   **Denis Firsanov<sup>1\*</sup>, Max Zacher<sup>1\*</sup>, Xiao Tian<sup>1</sup>, Yang Zhao<sup>1</sup>, John C. George<sup>2</sup>, Todd L. Sformo<sup>2</sup>, Greg**  
5   **Tomblin<sup>1</sup>, Seyed Ali Biashad<sup>1</sup>, Abbey Gilman<sup>1</sup>, Nicholas Hamilton<sup>1</sup>, Avnee Patel<sup>1</sup>, Maggie**  
6   **Straight<sup>1</sup>, Minseon Lee<sup>1</sup>, J. Yuyang Lu<sup>1</sup>, Ena Haseljic<sup>1</sup>, Alyssa Williams<sup>1</sup>, Nalani Miller<sup>1</sup>, Vadim N.**  
7   **Gladyshev<sup>3</sup>, Zhengdong Zhang<sup>4</sup>, Jan Vijg<sup>4, #</sup>, Andrei Seluanov<sup>1,5, #</sup>, Vera Gorbunova<sup>1,5, #</sup>**

8

9   <sup>1</sup>Department of Biology, University of Rochester, Rochester, NY, USA.

10   <sup>2</sup>Department of Wildlife Management, North Slope Borough, Utqiaġvik (Barrow), AK 99723, USA

11   <sup>3</sup>Division of Genetics, Department of Medicine, Brigham and Women's Hospital, Harvard Medical School,  
12   Boston, MA 02115, USA

13   <sup>4</sup>Department of Genetics, Albert Einstein College of Medicine, Bronx, NY 10461, USA

14   <sup>5</sup>Department of Medicine, University of Rochester Medical Center, Rochester, NY, USA

15   \*These authors contributed equally to this work.

16

17

18   #Corresponding authors:

19   Vera Gorbunova

20   University of Rochester

21   Email: vera.gorbunova@rochester.edu

22

23   Andrei Seluanov

24   University of Rochester

25   Email: andrei.seluanov@rochester.edu

26

27   Jan Vijg

28   Albert Einstein College of Medicine

29   Email: jan.vijg@einsteinmed.edu

30

31

32

33

34 **Abstract**

35 At over 200 years, the maximum lifespan of the bowhead whale exceeds that of all  
36 other mammals. The bowhead is also the second-largest animal on Earth, reaching  
37 over 80,000 kg<sup>1</sup>. In spite of its very large number of cells, the bowhead is not highly  
38 cancer-prone, an incongruity termed Peto's Paradox<sup>2</sup>. This has been explained by the  
39 evolution of additional tumor suppressor genes in larger animals, which is supported by  
40 research on elephants demonstrating expansion of the p53 gene<sup>3–5</sup>. However, we show  
41 here that bowhead whale fibroblasts undergo oncogenic transformation after disruption  
42 of fewer tumor suppressors than required for human fibroblasts. Instead, analysis of  
43 DNA repair revealed that bowhead cells repair double-strand breaks with uniquely high  
44 efficiency and accuracy compared to other mammals. Further, we identified two  
45 proteins, CIRBP and RPA2, that are present at high levels in bowhead fibroblasts and  
46 increase the efficiency and fidelity of DNA repair in human cells. These results suggest  
47 that rather than possessing additional tumor suppressor genes as barriers to  
48 oncogenesis, the bowhead whale relies on more accurate and efficient DNA repair to  
49 preserve genome integrity. This strategy that does not eliminate cells but repairs them  
50 may be critical for the long and cancer-free lifespan of the bowhead whale. Our work  
51 demonstrates the value of studying long-lived organisms in identifying novel longevity  
52 mechanisms and their potential for translation to humans.

53

54

55 **Introduction**

56 The Alaskan Iñupiat Inuit, who carry on a long tradition of subsistence hunting of the  
57 bowhead whale (*Balaena mysticetus*), maintain that these animals “live two human  
58 lifetimes”<sup>6</sup>. Remarkably, a series of bowhead whales captured in the late-twentieth and  
59 early-twenty-first centuries lent new credence to these claims, as embedded in their  
60 bodies were traditional stone harpoon points and bomb lance fragments dating to the  
61 Victorian era<sup>7</sup>. Subsequent scientific study and age estimation through quantification of

62 ovarian corpora, baleen dating, and eye lens aspartic acid racemization analysis  
63 supported a maximum lifespan exceeding 200 years in the bowhead whale<sup>7–12</sup>. Thus,  
64 the range of mammalian lifespans covers roughly 2 orders of magnitude, with the model  
65 organism *Mus musculus* living for 2-3 years while the bowhead whale lives 100 times as  
66 long.

67 An increased number of cells and cell divisions in larger organisms might be expected  
68 to contribute to increased cancer incidence and shorter lifespans. The apparent  
69 contradiction between expected and observed cancer rates in relation to species body  
70 mass has been noted for decades and is known as Peto's Paradox.<sup>2,13–15</sup> It is theorized  
71 to result from compensatory evolutionary adaptations driven by reduced extrinsic  
72 mortality in larger species<sup>2</sup>. The bowhead whale exceeds 80,000 kg in mass and 200  
73 years in lifespan. Both of these factors predispose it to accumulating large numbers of  
74 DNA mutations throughout life. To remain alive for so long it must possess uniquely  
75 potent genetic mechanisms to prevent cancer and other age-related diseases.

76 However, primary research publications on genetic and molecular mechanisms of aging  
77 in the bowhead whale are scarce, consisting primarily of genome and transcriptome  
78 analysis<sup>16–18</sup>.

79 The multi-stage model of carcinogenesis posits that the transition from a normal cell to a  
80 cancer cell involves multiple distinct genetic “hits,” or mutations<sup>19</sup>. Larger and longer-  
81 living species might require greater numbers of “hits” for oncogenic transformation,  
82 given their greater cell number and increased lifespan. Indeed, there is experimental  
83 evidence to support this hypothesis. Rangarajan et al. found that while mouse  
84 fibroblasts require perturbation of 2 pathways for tumorigenic transformation (p53 and

85 Ras), human fibroblasts require 5 hits (p53, pRb, PP2A, telomerase and Ras)<sup>20</sup>. A  
86 human should thus have a dramatically lower per-cell incidence of malignant  
87 transformation than a mouse, and can maintain a larger number of cells for a longer  
88 period of time.

89 Species that are larger and longer-lived than humans may be expected to have even  
90 more layers of protection against oncogenic transformation than humans and common  
91 model species. In support of this hypothesis, recent studies have identified copy number  
92 expansion and functional diversification of multiple tumor suppressor genes, such as  
93 *TP53* and *LIF*, in elephants and other taxa<sup>3,5,21–23</sup>. These studies identified multiple  
94 copies of *TP53* in the elephant genome, several of which were confirmed to be  
95 transcribed and translated in elephant fibroblasts and contributed to an enhanced  
96 apoptotic response to genotoxic stress.

97 However, additional copies of p53 genes are unlikely to slow down aging. One  
98 promising mechanism that could help explain both cancer resistance and slower aging  
99 in long-lived mammals is more accurate or efficient DNA repair. Genetic mutations have  
100 been identified as causal factors in carcinogenesis for over a century<sup>24</sup>. Perhaps one of  
101 the most compelling lines of evidence supporting the role of DNA repair in the  
102 pathogenesis of aging and cancer comes from studies of mutants with accelerated  
103 aging phenotypes. Remarkably, most such mutants have defects in DNA repair  
104 enzymes<sup>25–29</sup>. Across species, several studies have also pointed toward improved DNA  
105 repair capacity and reduced mutation accumulation as characteristics associated with  
106 species longevity<sup>30–34</sup>. Here, we identify specific cellular and molecular traits  
107 characterizing bowhead cancer resistance and longevity and distinguishing the

108 bowhead from shorter-lived mammals including humans. We show that bowhead whale  
109 cells are not more prone to apoptosis, and require fewer genetic hits for malignant  
110 transformation than human cells. Instead, the bowhead whale relies on more accurate  
111 and efficient DNA double strand break (DSB) repair mediated by CIRBP and RPA2.  
112 This more “conservative” strategy that does not needlessly eliminate cells but repairs  
113 them may be critical for the long and cancer-free lifespan of the bowhead whale.

114

## 115 **Results**

116 **Growth characteristics, cellular senescence, and cell death in bowhead whale**  
117 Most human somatic cells lack telomerase activity and as a result undergo replicative  
118 senescence with serial passaging in culture<sup>35</sup>. Replicative and stress-induced  
119 senescence are important mechanisms for preventing cancer. Using TRF and TRAP  
120 assays to measure telomere length and telomerase activity, we found that bowhead  
121 whale skin fibroblasts, like human fibroblasts, lack telomerase activity and experience  
122 telomere shortening followed by replicative senescence with passaging in culture  
123 (Figure 1a, b). In both species, nearly all cells stained positive for senescence-  
124 associated β-galactosidase upon terminal growth arrest (Figure 1c, d). As in human  
125 fibroblasts, stable overexpression of human telomerase reverse transcriptase (*hTERT*)  
126 to maintain telomere length prevented replicative senescence in bowhead cells (Figure  
127 1a). Senescence can also be induced by DNA damage. Like human cells, bowhead  
128 whale skin fibroblasts efficiently entered senescence but did not significantly induce cell  
129 death in response to 10 or 20 Gy of γ-irradiation (Figure 1c-e).

130 Interestingly, transcriptome analysis of human and bowhead whale senescent  
131 fibroblasts showed reduced induction of senescence-associated secretory phenotype  
132 (SASP) factors in bowhead whale (Figure 1f) relative to human. Paracrine effects of  
133 SASP on surrounding cells are thought to contribute to age-related diseases and  
134 carcinogenesis. These transcriptomic differences may indicate that senescence is able  
135 to preserve its anti-cancer function in the bowhead with reduced harmful paracrine  
136 signaling.

137 To test whether increased p53 activity could contribute to cancer resistance in the  
138 bowhead whale, we transiently transfected primary mouse, cow, human and bowhead  
139 whale skin fibroblasts with a luciferase reporter vector containing a p53-response  
140 element. The bowhead whale cells had the lowest p53 activity of the species tested  
141 (Figure 1g). Additionally, we did not observe any differences in the induction of  
142 apoptosis in response to UVC between species (Figure 1h). Together, our results argue  
143 against the idea that increased clearance of damaged cells through apoptosis  
144 contributes to cancer resistance in the bowhead whale.

145 **Requirements for oncogenic transformation of bowhead whale cells**

146 We initially identified a minimal combination of oncogene and tumor suppressor hits  
147 required for *in vitro* malignant transformation of bowhead whale skin fibroblasts using  
148 the soft agar assay, which measures anchorage-independent growth, a hallmark of  
149 cancer. While normal cells undergo growth arrest or programmed cell death (anoikis) in  
150 soft agar, malignant cells continue to grow without substrate adhesion and form visible  
151 colonies<sup>36</sup>. We introduced constructs targeting oncogene and tumor suppressor  
152 pathways into primary skin fibroblasts with PiggyBac (PB) transposon vectors, which

153 integrate into the genome and drive stable expression. Since bowhead whale primary  
154 fibroblasts, like human fibroblasts, exhibit progressive telomere shortening and lack  
155 telomerase activity (Figure 1b), we used cell lines expressing (*hTERT*) to bypass  
156 replicative senescence.

157 In agreement with published findings, transformation of human *hTERT*+ fibroblasts  
158 required combined expression of H-Ras<sup>G12V</sup>, SV40 Large T (LT) antigen (which binds  
159 and inactivates p53 and the Rb family of tumor suppressors), and SV40 Small T (ST)  
160 antigen (which binds and inactivates PP2A) (Figure 2a)<sup>20</sup>. Rather than requiring hits to  
161 additional pathways, however, bowhead *hTERT*+ fibroblasts were transformed by H-  
162 Ras<sup>G12V</sup> and SV40 LT alone, suggesting that bowhead cells may require fewer genetic  
163 mutations to become cancerous compared to human cells (Figure 2a). These findings  
164 were supported by mouse xenograft assays, in which the number of hits needed for  
165 tumor growth matched the findings from soft agar (Figure 2b).

166 We next sought to confirm these findings at the genetic level, through CRISPR editing  
167 of individual tumor suppressor genes in bowhead fibroblasts. While the sequenced  
168 bowhead genome has not revealed copy number expansion of canonical tumor  
169 suppressor genes<sup>16,17</sup>, CRISPR knockout allows for more precise quantification of the  
170 number of genetic mutations required for oncogenesis. While the most important target  
171 of SV40 LT is thought to be Rb (*RB1* gene), it is also known to inactivate p130 and  
172 p107, two additional members of the Rb-family, providing some level of functional  
173 redundancy. Using CRISPR, we were able to introduce targeted mutations into the  
174 bowhead *RB1* gene specifically, along with *TP53* (the other target of LT), and *PTEN* (an  
175 upstream inhibitor of Akt signaling commonly mutated in human cancers, and operating

176 in the same pathway as PP2A). Following transfection of *hTERT*+ bowhead fibroblasts  
177 with Cas9-guide RNA ribonucleoprotein complexes targeting each of the  
178 aforementioned genes, we screened clonally isolated colonies for loss of the targeted  
179 protein by Western blot (Figure 2c, d, Extended Data Figure 1a, b). We additionally  
180 screened the colonies with luciferase reporter assays to confirm loss of protein function  
181 and activity (Extended Data Figure 1c, d). For each selected clone, we sequenced the  
182 CRISPR-targeted genes to confirm homozygous knockout at the genetic level and  
183 determine the causal mutations (Supplementary Figure 1, 2). Through this strategy, we  
184 generated single and compound homozygous knockout bowhead whale fibroblasts for  
185 *TP53*, *RB1*, and *PTEN*. In agreement with our initial findings, genetic inactivation of  
186 *TP53* and *RB1* in bowhead whale fibroblasts expressing *hTERT* and H-Ras<sup>G12V</sup> was  
187 sufficient for malignant transformation in both soft agar and mouse xenograft assays  
188 (Figure 2a, b). These findings suggest that despite its large size and long lifespan, the  
189 cells of the bowhead whale unexpectedly require fewer mutational hits for malignant  
190 transformation than human cells.

## 191 **Excision repair and mutagenesis in the bowhead whale**

192 To understand if improved DNA repair might reduce cancer risk in the bowhead whale,  
193 we first assessed the efficiency of nucleotide excision repair (NER) and base excision  
194 repair (BER) in bowhead whale cells. NER is primarily responsible for removing helix-  
195 distorting DNA lesions. To quantify NER activity, we utilized a host cell plasmid  
196 reactivation assay and quantitation of cyclobutane pyrimidine dimers by ELISA to  
197 measure repair of UVC-induced DNA damage. NER efficiency was similar between  
198 bowhead and human (Extended Data Figure 2a, b). BER is responsible for ameliorating

199 many types of spontaneous DNA base damage such as oxidation and deamination. The  
200 efficiency of BER, as measured by plasmid reactivation assay, trended toward higher  
201 BER activity in bowhead whale compared to human cells, but this difference was not  
202 statistically significant (Extended Data Figure 2c). Additionally, bowhead fibroblasts  
203 displayed dramatically higher PARP activity in response to H<sub>2</sub>O<sub>2</sub> treatment (Extended  
204 Data Figure 2d, e). PARP proteins play important roles in the DNA damage response  
205 and are recruited to sites of DNA damage where they participate in the DNA damage  
206 response and in repair.

207 We next compared the point mutation frequency in the bowhead whale and human  
208 using the HPRT mutagenesis assay, which relies on loss of HPRT activity after  
209 mutagen treatment<sup>37</sup>. The *HPRT* gene exists as a single copy on the X chromosome in  
210 male mammalian cells, a feature we found to be true for the bowhead as well (see  
211 Methods). We treated primary fibroblast lines from male bowhead whale and human  
212 with the potent mutagen and alkylating agent N-ethyl-N-nitrosourea (ENU), and then  
213 plated cells in selective media containing 6-thioguanine, which kills cells with functional  
214 HPRT. Despite a slightly higher sensitivity to ENU in bowhead whale as indicated by  
215 colony-forming efficiency in non-selective media, the rate of HPRT mutant colony  
216 formation was markedly lower in bowhead whale than human fibroblasts, an effect  
217 which remained significant after adjusting for plating efficiency (Extended Data Figure  
218 2f, g). This result suggests that bowhead whale has more accurate DNA repair.

219 **High efficiency and fidelity of bowhead whale double-strand break repair**  
220 DNA DSBs are toxic if not repaired and may lead to mutations through inaccurate  
221 repair. DSBs are repaired by two major pathways: non-homologous end joining (NHEJ)

222 and homologous recombination (HR). To assess relative NHEJ efficiency, we integrated  
223 fluorescent GFP-based reporter cassettes<sup>38</sup> into fibroblasts from mouse, cow, human  
224 and bowhead whale. Following DSB induction with I-SceI, we observed markedly  
225 elevated NHEJ efficiency in bowhead whale relative to other species (Figure 3a,  
226 Extended Data Figure 3a-c). Additionally, bowhead whale fibroblasts accumulated fewer  
227 micronuclei, a marker of chromosomal instability, after 2Gy  $\gamma$ -irradiation (Figure 3b,  
228 Extended Data Figure 3d). The kinetics of radiation-induced DSB rejoicing as measured  
229 by pulsed-field gel electrophoresis were similar between bowhead and human cells,  
230 with almost all breaks repaired within 48h in both species (Extended Data Figure 3e, f).  
  
231 As mutations resulting from inaccurate DSB repair promote cancer development, we  
232 next sought to assess the fidelity of DSB repair in the bowhead whale. Sequencing and  
233 analysis of repair junctions from integrated NHEJ reporter (Figure 3) and extra-  
234 chromosomal NHEJ reporter (Extended Data Figure 3a, c) assays showed higher  
235 fidelity of NHEJ in bowhead whale cells: compared to human, the bowhead whale is  
236 less prone to producing deletions during the repair of incompatible DNA termini and far  
237 more frequently joins ends without deleting any bases beyond the small overhang  
238 region.

239 We also measured the fidelity of repair at an endogenous genomic locus. Initial  
240 sequencing results from CRISPR tumor suppressor knockout experiments suggested a  
241 strong bias in bowhead whale cells toward DSB repair products with single-base  
242 insertion mutations, in contrast to the greater diversity and size of repair outcomes  
243 commonly observed in human and mouse cells. To systematically compare mutational  
244 outcomes of CRISPR break repair in the bowhead whale to those of humans and

245 shorter-living mammals, we performed CRISPR transfections in multiple primary  
246 fibroblast lines from bowhead whale, human, cow, and mouse, and used deep amplicon  
247 sequencing of the targeted locus to generate detailed profiles of repair outcomes. We  
248 took advantage of the fact that exon 1 of the *PTEN* tumor suppressor gene is highly  
249 conserved across mammals, with 100% sequence identity across included species  
250 (Extended Data Figure 4a). We were therefore able to examine species-specific DSB  
251 repair outcomes at an endogenous genomic locus while minimizing intra-species  
252 variation in the break-proximal sequence context.

253 Analysis of sequencing data revealed species-specific repair outcomes, which were  
254 consistent across cell lines derived from multiple animals of each species (Figure 3d-f).  
255 In human, cow, and mouse, the most common mutational outcomes were deletions. In  
256 contrast, the bowhead was the only species that preferentially repaired breaks with a  
257 single-base insertion. The frequency of unmodified alleles, which are known to occur  
258 after error-free repair of CRISPR DSBs<sup>39,40</sup>, was the highest in bowhead whale (Figure  
259 3e). No insertions or deletions were detected in untreated control samples (Extended  
260 Data Figure 4b). As analysis of CRISPR RNP transfection efficiency by flow cytometry  
261 and cleavage efficiency by digital droplet PCR showed similar CRISPR efficiencies  
262 across species (Extended Data Figure 5a, Supplementary Figure 3a, b), differences in  
263 the unmodified allele fraction most likely result from differences in repair fidelity. While  
264 small indels predominated in all species, we observed a marked inverse correlation  
265 between the frequency of large deletions and species lifespan, with the bowhead  
266 producing fewer large deletions than human, cow, and mouse (Figure 3d-f). When we  
267 assigned frequency-based percentile ranks from most negative to most positive indel

268 size (largest deletions to largest insertions), we observed a strong correlation between  
269 species lifespan and 5th percentile indel size, corresponding to large deletions  
270 (Pearson's  $r=0.85$ ,  $p=0.0009$ ) (Extended Data Figure 6). The results from these  
271 experiments suggest a greater efficiency and accuracy of DSB repair in the bowhead  
272 whale relative to humans and other mammals.

273 **CIRBP contributes to high DSB repair efficiency in the bowhead whale**

274 To identify mechanisms contributing to the efficiency and accuracy of DSB repair in the  
275 bowhead whale, we measured and compared expression of DNA repair proteins in the  
276 bowhead to other mammalian species by Western blot, quantitative MS proteomics, and  
277 RNA seq (Figure 4a, Extended Data Figure 7a-d). Bowhead cells showed strikingly  
278 higher abundance of cold-inducible RNA-binding protein (CIRBP) than other  
279 mammalian species. (Figure 4a, Extended Data Figure 7a, d). Levels of PARP1, a  
280 functional partner of CIRBP during DNA repair<sup>41</sup>, were also increased relative to human.  
281 Unexpectedly, we found that levels of several important canonical NHEJ proteins (e.g.  
282 Ku70, Ku80, DNA-PKcs) are substantially higher in human cells than any other species  
283 tested (Figure 4a, Extended Data Figure 7a).

284 CIRBP is an RNA- and PAR-binding protein whose expression is induced by a variety of  
285 cellular stressors including cold shock, hypoxia, and UV irradiation<sup>41-44</sup>. It binds the 3'  
286 UTR of mRNAs that encode proteins involved in cellular stress and DNA damage  
287 responses and promotes their stability and translation: known targets include ATR,  
288 RPA2, thioredoxin, and p27<sup>45-48</sup>. There is also evidence for a more direct role of CIRBP  
289 in DNA repair: PARP-1-dependent localization of CIRBP to sites of DNA damage  
290 promotes DSB repair and antagonizes micronucleus formation<sup>41</sup>.

291 To test whether CIRBP contributes to efficient NHEJ in bowhead whale cells, we  
292 overexpressed human (hCIRBP) and bowhead whale (bwCIRBP) in human NHEJ  
293 reporter cells. Overexpression of bwCIRBP, but not hCIRBP, enhanced NHEJ efficiency  
294 in human cells ~1.6-fold ( $p=0.002$ ) and in mouse embryonic fibroblasts ~3-fold (Figure  
295 4b, Extended Data Figure 8a). Overexpression of bwCIRBP, but not hCIRBP, also  
296 increased HR efficiency in human cells ~2-fold (Figure 4c, e). Conversely, CIRBP  
297 depletion in bowhead whale cells by siRNA significantly reduced NHEJ efficiency  
298 ( $p=0.032$ ) (Figure 4d, e). Consistent with published observations, overexpression of  
299 bwCIRBP with nine arginines in the repeated RGG motif mutated to alanine (9R/A),  
300 which impairs CIRBP's ability to bind to PAR-polymers<sup>41</sup>, failed to stimulate HR and  
301 reduced stimulation of NHEJ (Figure 4b, c, e). To test the effects of bwCIRBP  
302 overexpression on chromosomal stability, we quantified formation of micronuclei in  
303 human cells after  $\gamma$ -irradiation. We found that overexpression of bwCIRBP significantly  
304 decreased the percentage of cells with micronuclei, reflecting an improvement in  
305 genomic stability (Figure 4f).

306 Surprisingly, we observed during our experiments that CIRBP protein abundance in the  
307 bowhead remained high regardless of whether cells were cultured at 37°C, 33°C, or  
308 lower temperatures (the core body temperature of the bowhead has been measured at  
309 33.8°C)<sup>49,50</sup>, suggesting constitutive expression in contrast to its strong temperature  
310 dependence in other mammals (Extended Data Figure 8b)<sup>42</sup>. At no temperature did  
311 human cells produce similarly high CIRBP levels. In contrast, RNA-seq analysis  
312 (verified by qPCR) showed nearly identical CIRBP transcript levels between human and  
313 bowhead whale fibroblasts (Extended Data Figure 7b, 8c). The discrepancy between

314 mRNA and protein levels in tested species agrees with previous findings of CIRBP  
315 regulation at the post-transcriptional level<sup>51,52</sup>.

316 The human and bowhead CIRBP proteins differ by only 5 C-terminal amino acids  
317 (Extended Data Figure 9a, b). Substitution of these 5 codons in hCIRBP with bowhead  
318 codons increased protein expression, while mutation of bwCIRBP with the 5 hCIRBP  
319 codons decreased it (Extended Data Figure 9c). This was not accompanied by changes  
320 in mRNA transcript levels, consistent with post-transcriptional regulation (Extended Data  
321 Figure 9d). Interestingly, although CIRBP abundance increased following introduction of  
322 the 5 bowhead substitutions to hCIRBP, it did not achieve the expression of bowhead  
323 CIRBP, suggesting that synonymous changes to the mRNA coding sequence contribute  
324 to higher translation efficiency of bowhead whale CIRBP. Consistent with this notion,  
325 bwCIRBP has a higher codon adaptation index (CAI)<sup>53</sup> than hCIRBP; this difference  
326 remains after introduction of the five reciprocal mutations (Extended Data Figure 9e).

327 To test whether a hypothermia-mediated increase in human CIRBP can also affect DSB  
328 repair efficiency, we kept human cells for two days at 33°C before transfection with  
329 NHEJ reporter plasmid pre-digested with I-Sce-1. Indeed, cells exposed to hypothermia  
330 showed a ~2-fold ( $p=0.0017$ ) increase in NHEJ efficiency (Figure 4g).

331 **Mechanisms of bowhead whale DNA repair fidelity**

332 LC-MS proteomics data and Western blots with multiple antibodies suggested increased  
333 abundance of the single-stranded DNA binding protein RPA2 in the bowhead whale  
334 (Figure 4a, Extended Data Figure 7a, c). This was paralleled by elevated RPA2  
335 transcript abundance (Extended Data Figure 7b). RPA is a conserved heterotrimeric

336 ssDNA-binding protein complex required for eukaryotic DNA replication, which plays a  
337 critical role in DNA repair and DNA damage signaling<sup>54,55</sup>. RPA deficiency increases the  
338 frequency of DSBs under both basal<sup>56</sup> and stressed<sup>57</sup> conditions. Conversely, RPA  
339 overexpression increases resistance to genotoxic insults<sup>57–60</sup>. RPA promotes NHEJ *in*  
340 *vitro*<sup>61</sup>, can protect ssDNA overhangs at Ku-bound DSBs<sup>62,63</sup>, and antagonizes  
341 microhomology-mediated end joining<sup>64,48,49</sup>.

342 It has previously been shown that RPA2 is an unstable protein highly prone to oxidative  
343 damage, and that the abundance of this subunit affects the abundance of RPA1 and  
344 RPA3<sup>65,66</sup>. We therefore sought to determine whether the high abundance of RPA2 in  
345 bowhead whale cells may contribute to DNA repair fidelity. Because RPA is required for  
346 cell viability, and can cause toxicity when not expressed with appropriate subunit  
347 stoichiometry<sup>67</sup>, we selected methods aimed at transiently increasing or decreasing  
348 RPA activity in the period surrounding break induction to specifically isolate effects on  
349 DSB repair fidelity. Treatment of cells transfected with CRISPR to induce DSBs with the  
350 small-molecule RPA DNA-binding inhibitor TDRL-505<sup>68</sup> significantly increased indel  
351 rates in both bowhead and human fibroblasts (Figure 5a, b). In bowhead, RPA inhibition  
352 also increased the frequency of larger deletions, although this difference did not reach  
353 significance (Figure 5b). Conversely, co-transfection of trimeric recombinant human  
354 RPA protein during CRISPR significantly decreased the frequency of mutated alleles in  
355 human cells without affecting CRISPR RNP transfection efficiency (Figure 5a,  
356 Supplementary Figure 3c). We additionally tested the effect of bwCIRBP  
357 overexpression on repair fidelity in human cells and observed a modest but significant  
358 reduction in indel rates (Figure 5c). These results support the notion that variations in

359 CIRBP and RPA2 abundance, affect the fidelity of DSB repair and promote genomic  
360 stability in the bowhead whale.

361

362 **Discussion**

363 By studying a mammal capable of maintaining its health and avoiding death from cancer  
364 for over 2 centuries, we are offered a unique glimpse behind the curtain of a global  
365 evolutionary experiment that tested more mechanisms affecting cancer and aging than  
366 humans could ever hope to approach. Through experiments using primary fibroblasts  
367 from the bowhead whale, we experimentally determined genetic requirements for  
368 oncogenic transformation in the world's longest living mammal, and provide evidence  
369 that additional tumor suppressors are not the only solution to Peto's Paradox. Instead,  
370 we find that the bowhead whale solution lies upstream of tumor suppressor loss, and is  
371 defined by a capacity for highly accurate DNA DSB repair. We also present evidence  
372 that two proteins, RPA2 and CIRBP, are highly expressed in the bowhead relative to  
373 other mammals and contribute to more efficient and accurate DSB repair.

374 When cells experience DNA breaks, they are faced with a choice between several  
375 different fates, which cooperate to balance short-term risks to organismal viability with  
376 the long-term risks of genome instability. One option is resolution of the DNA damage  
377 response and resumption of cell function. While an unrepairs DSB is sufficient to kill a  
378 cell, an inaccurately repaired DSB can give rise to a cancer that kills the entire  
379 organism. The magnitude of this threat is reflected in the diversity of checkpoint  
380 mechanisms mammals have evolved to arrest or eliminate cells with DNA damage.

381 Thus, persistent or excessive damage signaling can trigger a second category of DNA  
382 damage outcomes: apoptosis or senescence.

383 Prompt and efficient DSB repair promotes the survival and continued function of  
384 somatic cells. Ideally, this results in faithful restoration of the original genomic  
385 sequence. However, aberrant outcomes such as loss of chromosome fragments (e.g.  
386 micronuclei), chromosomal rearrangements, or large deletions cause massive changes  
387 to the original DNA sequence<sup>69</sup>. These forms of genome instability are hallmarks of  
388 cancer and core drivers of malignant transformation. In quiescent cell populations, there  
389 is increased potential for accumulation of persistent unrepaired DSBs. Efficient repair of  
390 DSBs is particularly important for permanently post-mitotic cells like neurons and  
391 cardiomyocytes, which often are not replaced after cell death. Ultimately, the value of  
392 DSB repair to an organism's survival is a function of both accuracy and efficiency. Upon  
393 excessive damage, it is often better for organismal survival and longevity to eliminate  
394 cells at risk of genomic instability through apoptosis or senescence.

395 Senescence is an important mechanism to control cells with potential genome instability  
396 through permanent growth arrest. Telomere shortening functions to induce senescence  
397 by limiting the number of times a cell can replicate. This mechanism appears to be  
398 functional in bowhead whale fibroblasts, in line with the theory that telomere shortening  
399 is prevalent as a cancer-prevention mechanism in large-bodied mammals<sup>70</sup>. An  
400 additional such mechanism was recently reported for the bowhead whale in the form of  
401 a *CDKN2C* checkpoint gene duplication<sup>71</sup>. Senescence in general appears to represent  
402 a tradeoff between cancer and other forms of age-related dysfunction. There is  
403 substantial evidence for harmful paracrine effects of senescence through the pro-

404 inflammatory SASP<sup>72</sup>. Here we demonstrate that bowhead whale has reduced  
405 inflammatory components of the SASP, which could reduce the negative impact of  
406 senescence.

407 Like senescence, apoptosis is an efficient and critical mechanism to reduce the number  
408 of cells with dangerous levels of genome instability. Its importance as a cancer  
409 prevention mechanism is evident from the prevalence of p53 mutations in cancer<sup>73</sup> and  
410 supported by findings of enhanced p53 function in the elephant<sup>3–5</sup>. However, high rates  
411 of apoptosis are likely to accelerate age-related decline through permanent cell loss<sup>74</sup>,  
412 especially in post-mitotic and irreplaceable cell populations in tissues such as brain and  
413 heart. Because excessive cell death or arrest is incompatible with organismal survival,  
414 baseline levels of DNA damage must be repaired. Given that most cells in mammalian  
415 bodies experience multiple endogenous DSBs per day<sup>75</sup>, faithful repair of these breaks  
416 is critical.

417 Why might the bowhead whale have evolved improved DNA repair, as opposed to the  
418 increased tumor suppressor copy number and elevated apoptotic response found in the  
419 elephant and often proposed as a solution to Peto's Paradox? One possible explanation  
420 is that tumor suppressors, apoptosis, and senescence all appear to pose costs to the  
421 organism and represent tradeoffs between cancer and stem cell depletion leading to  
422 age-related degeneration. Simply shifting the balance from apoptosis/senescence to  
423 survival and repair could be detrimental if not also coupled with increased fidelity, as  
424 evidenced by the frequent upregulation of DNA repair pathways in cancer cells<sup>76</sup>.  
425 However, evolutionary improvements that couple high efficiency with high fidelity, as  
426 found in the bowhead whale, would promote long-term tissue function and maintenance

427 at both the cellular and genomic levels. Efficient repair could reduce loss of valuable  
428 post-mitotic cells with age and reduce mutations in dividing cells. Maintenance of  
429 genome stability would reduce cancer risk and - as suggested by a rapidly growing body  
430 of evidence implicating age-related somatic mosaicism as a ubiquitous feature and  
431 functional driver of aging<sup>77-81</sup>- likely also protect against numerous other aspects of age-  
432 related decline. Thus, the lower accuracy and efficiency of DSB repair observed in  
433 mammals with shorter lifespans may simply reflect an absence of sufficient selective  
434 pressure. One potential drawback of a very accurate DNA repair system is a reduction  
435 in diversity and slower rate of evolution of new traits. However, species living in safe  
436 and stable environments have no evolutionary pressure to rapidly evolve new  
437 adaptations. Interestingly, genome analysis of long-lived rockfishes living in deep ocean  
438 revealed positive selection in DNA repair pathways<sup>82</sup>.

439 The evolution of constitutively high CIRBP expression in the bowhead whale is likely to  
440 have been driven, at least in part, by the unique physiological stresses this Arctic  
441 cetacean must endure. This naturally includes the extremely cold water in which it is  
442 constantly immersed, but also the ischemia/reperfusion-like fluctuations in tissue  
443 oxygen concentrations experienced by diving mammals<sup>83</sup>.

444 Interestingly, beneficial effects of cold as a therapeutic agent have been known for a  
445 long time with brief cold-water immersion believed to promote health and hardening in  
446 Nordic cultures. Currently, whole body cryotherapy is widely used in sports medicine to  
447 reduce inflammation and facilitate recovery after exercise or injury<sup>84</sup>. While molecular  
448 mechanisms responsible for the beneficial effects of cryotherapy are largely unknown,

449 we speculate that increased CIRBP expression may contribute to health benefits by  
450 facilitating DNA repair.

451 Cold showers provide a mild and transient reduction in body temperature, whereas  
452 artificial reduction of body temperature, or therapeutic hypothermia, is used clinically  
453 during surgery<sup>85</sup>. Interestingly, recovery from therapeutic hypothermia is compromised  
454 in CIRBP-KO rats and improved in rats with transgenic CIRBP overexpression<sup>86</sup>. Similar  
455 protective effects of CIRBP during hypothermia have been reported in brain<sup>87</sup>, kidney<sup>88</sup>  
456 intestine<sup>89</sup>, and cold-preserved hearts<sup>90</sup>. Given the dramatically enhanced protein  
457 production driven by bwCIRBP and hCIRBP mutants, local delivery of such CIRBP  
458 variants (e. g. through mRNA/DNA vector injection) could hold promise as strategies to  
459 improve tissue recovery from surgery or organ transplant.

460 There are currently no approved therapeutics which aim to bolster DNA repair for the  
461 prevention of cancer or age-related decline, and it has been suggested that DNA repair  
462 would be difficult or impossible to improve<sup>91</sup>. However, the bowhead whale provides  
463 evidence that this notion is incorrect. Therapeutics based on increasing the activity or  
464 abundance of proteins like CIRBP or RPA2 could one day enable the treatment of  
465 genome instability as a modifiable disease risk factor.

466

## 467 Acknowledgements

468 We would like to thank the researchers at the North Slope Borough Department of  
469 Wildlife Management, the Alaska Eskimo Whaling Commission, and the Iñupiaq  
470 community of Barrow for generously sharing bowhead whale samples, time, resources,

471 skill, and knowledge, and without whom the above work would not have been possible.

472 This work was supported by grants from US National Institutes on Aging to VNG, ZZ,

473 JV, AS and VG, and by an award from the Milky Way Research Foundation to VG.

474

475 **Author contributions**

476 VG, AS, DF, MZ designed research; DF analyzed senescence, DNA repair, CIRBP with  
477 help from SAB, AP, EH, AW, NM; MZ conducted tumor suppressor CRISPR  
478 experiments, RPA experiments, HPRT assays, and assessed DNA repair fidelity using  
479 CRISPR with help from SB, MS, NH; XT analyzed tumorigenicity; YZ and AG assisted  
480 with mouse tumor studies; JCG, TLS, MZ, DF collected bowhead specimens; MZ, GT  
481 performed proteomics; ML analyzed micronuclei; JYL analyzed SASP; VG, ZZ, JV  
482 contributed data analysis and conceptualization; VG and AS obtained funding and  
483 supervised the study; MZ, DF, AS and VG wrote the manuscript with input from all  
484 authors.

485

486 **Competing interests**

487 The authors declare no competing interests.

488

489 **Methods**

490 **Reagents**

491 Detailed information on reagents, such as antibodies and sequences of primers, probes,  
492 CRISPR guides, and siRNAs, is provided in Supplementary Methods.

493 **Animal experiments**

494 All animal experiments were approved and performed under pre-approved protocols  
495 and in accordance with guidelines set by the University of Rochester Committee on  
496 Animal Resources (UCAR).

497 **Whale sample collection**

498 Bowhead whale tissues were obtained from adult bowhead whales (*Balaena*  
499 *mysticetus*) captured during 2014 and 2018 Iñupiaq subsistence harvests in Barrow  
500 (Utqiāġvik), AK, in collaboration with the North Slope Borough Department of Wildlife  
501 Management (NSB DWM) and Alaska Eskimo Whaling Commission after signing a  
502 Memorandum of Understanding (September 2014 and March 2021). Tissues were  
503 sampled immediately after bowhead whales were brought ashore, after permission to  
504 sample was given by the whaling captain, and explants kept in culture medium on ice or  
505 at 4°C through initial processing and shipping until arrival at the University of Rochester  
506 (UR) for primary fibroblast isolation from skin and lung. Transfer of bowhead whale  
507 samples from NSB DWM to UR was under NOAA/NMFS permit 21386.

508 **Primary cell cultures**

509 Primary skin fibroblasts were isolated from skin (dermal) tissues as previously  
510 described.<sup>92</sup> Briefly, skin tissues were shaved and cleaned with 70% ethanol. Tissues  
511 were minced with a scalpel and incubated in DMEM/F-12 medium (ThermoFisher) with  
512 Liberase<sup>TM</sup> (Sigma) at 37°C on a stirrer for 15-90 min. Tissues were then washed and  
513 plated in DMEM/F-12 medium containing 12% fetal bovine serum (GIBCO) and  
514 Antibiotic-Antimycotic (GIBCO). All subsequent maintenance culture for fibroblasts from  
515 bowhead and other species was in EMEM (ATCC) supplemented with 12% fetal bovine  
516 serum (GIBCO), 100 units/mL penicillin, and 100 mg/mL streptomycin (GIBCO). All  
517 primary cells were cultured at 37°C with 5% CO<sub>2</sub> and 3% O<sub>2</sub> except bowhead whale  
518 cells, which were cultured at 33°C with 5% CO<sub>2</sub> and 3% O<sub>2</sub> based on published field  
519 measurements of bowhead body temperature, which measured a core temperature of  
520 33.8 °C and a range of lower temperatures in muscle and peripheral tissue.<sup>49,50</sup> Prior to  
521 beginning experiments with bowhead whale fibroblasts, optimal growth and viability  
522 conditions were empirically determined through testing of alternative temperatures,  
523 serum concentrations, and cell culture additives, with optimal culture medium found to  
524 be the same for bowhead and other species. Following isolation, low population-  
525 doubling (PD) primary cultures were preserved in liquid nitrogen, and PD was  
526 continually tracked and recorded during subsequent use for experiments.

527 **Soft agar assay**

528 Fibroblast culture medium as described above was prepared at 2X concentration using  
529 2X EMEM (Lonza). To prepare the bottom layer of agar plates, 2X medium was mixed  
530 with a sterile autoclaved solution of 1.2% Noble Agar (Difco) at a 1:1 volumetric ratio,  
531 and 3 mL of 1X medium/0.6% agar was pipetted into each 6-cm cell culture dish and

532 allowed to solidify at room temperature in a tissue culture hood. To plate cells into the  
533 upper layer of soft agar, cells were harvested and washed, and immediately prior to  
534 plating were resuspended in 2X medium at 20,000 cells/1.5 mL and diluted twofold in  
535 0.8% Noble Agar pre-equilibrated to 37°C. The cells in 0.4% agar/1X medium were  
536 pipetted gently to ensure a homogeneous single cell suspension, and 3 mL (20,000  
537 cells) per 6 cm dish were layered on top of the solidified lower layer. After solidifying in  
538 tissue culture hoods for 20-30 min, additional medium was added to ensure the agar  
539 layers were submerged, and dishes were moved into cell culture incubators. Fresh  
540 medium was added onto the agar every 3 days. 4 weeks after plating, viable colonies  
541 were stained overnight with nitro blue tetrazolium chloride (Thermo Fisher) as  
542 previously described.<sup>36</sup> All cell lines were plated in triplicate.

543 **Mouse xenograft assay**

544 NIH-III nude mice (Crl:NIH-Lystbg-J Foxn1nuBtkid) were purchased from Charles  
545 River Laboratories Inc. (Wilmington, MA, USA). Seven-week-old female mice were used  
546 to establish xenografts. For each injection,  $2 \times 10^6$  cells were harvested and  
547 resuspended in 100 µl of ice-cold 20% matrigel (BD Bioscience, Franklin Lakes, NJ) in  
548 PBS (Gibco). Mice were anesthetized with isoflurane gas, and 100 µl solution per  
549 injection was injected subcutaneously into the right and left flanks of each mouse with a  
550 22 gauge needle. 3 mice were injected bilaterally, for a total of 6 injections, per cell line  
551 tested. Tumor length and width were measured and recorded every 3-4 days. Mice  
552 were euthanized after reaching a predetermined humane tumor burden endpoint of a  
553 maximum tumor dimension of 20mm in diameter, determined by the longest dimension  
554 of the mouse's largest tumor. For mice that did not reach tumor burden endpoints,

555 experiments were terminated and mice euthanized after a maximum of 60 days.  
556 Euthanized mice were photographed and tumors were excised, photographed, and  
557 weighed to determine the mass of each tumor. Sections of each tumor were frozen at -  
558 80°C and preserved in formalin.

559 **Telomere lengths**

560 Telomere length was analyzed by Southern blot using the TRF method. Genomic DNA  
561 was extracted from cultured fibroblasts at different population doublings, digested with a  
562 mixture of Alul, HaeIII, Rsal, and Hinfl restriction enzymes that do not cut within  
563 telomeric repeat sequences, separated using pulsed-field gel electrophoresis, and  
564 hybridized with a radiolabeled oligonucleotide containing telomeric sequence  
565 (TTAGGG)<sub>4</sub>. Pulsed field gels were run using a CHEF-DR II apparatus (Bio-Rad) for  
566 22h at a constant 45 V, using ramped pulse times from 1 to 10 s.

567 **Telomeric repeat amplification protocol**

568 Telomeric repeat amplification protocol assay was performed using the TRAPeze kit  
569 (Chemicon, Temecula, CA, USA) according to manufacturer instructions. Briefly, in the  
570 first step of the TRAP assay, radiolabeled substrate oligonucleotide is added to 0.5 µg  
571 of protein extract. If telomerase is present and active, telomeric repeats (GGTTAG) are  
572 added to the 3' end of the oligonucleotide. In the second step, extended products are  
573 amplified by PCR. Telomerase extends the oligonucleotide by multiples of 6 bp,  
574 generating a ladder of products of increasing length. A human cancer cell line  
575 overexpressing telomerase as well as rodent cells were used as a positive control.

576 **CRISPR ribonucleoprotein transfection**

577 CRISPR RNP complexes were formed in vitro by incubating Alt-R™ S.p.Cas9 Nuclease  
578 V3 (Integrated DNA technologies) with tracRNA annealed to target-specific crRNA  
579 (Integrated DNA Technologies) according to manufacturer instructions. For generation  
580 of tumor suppressor knockouts, 3 RNP complexes with crRNAs targeting different sites  
581 in a single target gene were combined and Alt-R Cas9 Electroporation Enhancer  
582 (Integrated DNA Technologies) was added to transfection mixes prior to electroporation.  
583 For comparative analysis of repair fidelity, 3 µg of pmaxGFP plasmid (Lonza) was  
584 added to transfection mixes to monitor transfection efficiency. Cells were trypsinized  
585 and washed with PBS, and  $1 \times 10^6$  cells were resuspended in 100 µL of NHDF  
586 Nucleofector Solution (Lonza). The cell suspension was then combined with the  
587 CRISPR transfection solution and gently mixed prior to electroporation on an Amaxa  
588 Nucleofector 2b (Lonza) using program U-23. For RPA inhibition, human and bowhead  
589 fibroblasts were treated with 50 uM TDRL-505 (Sigma) (diluted 1000x into culture  
590 medium from 50mM stock solution in DMSO) for 3 hours prior to CRISPR transfection  
591 and kept in medium with 50 uM TDRL-505 for 18 hours after transfection. For RPA co-  
592 transfection, 1 µg of recombinant human RPA heterotrimer (Enzymax) was added to  
593 CRISPR transfection solution immediately prior to electroporation.

594 **Isolation of clonal cell colonies and screening for tumor suppressor knockout**

595 Following CRISPR transfection, cells were plated at low density in 15-cm dishes to  
596 allow for the formation of isolated colonies. Once clonal colonies of sufficient size had  
597 formed, positions of well-isolated colonies were visually marked on the bottom of the  
598 cell culture dish while under a microscope using a marker. Dishes were aspirated and  
599 washed with PBS. Forceps were used to dip PYREX® 8x8 mm glass cloning cylinders

600 in adhesive Dow Corning® high-vacuum silicone grease (Millipore Sigma) and one  
601 glass cylinder was secured to the dish over each marked colony. 150 µL of trypsin was  
602 added to each cylinder and returned to the incubator. When cells had rounded up from  
603 the plate, the trypsin in each cylinder was pipetted to detach cells and each colony was  
604 added to a separate well in a 6-cm culture dish containing culture medium. After  
605 colonies were expanded and split into 2 wells per colony, one well was harvested for  
606 Western blot screening for absence of target proteins, while the remaining well was kept  
607 for further experiments.

608 **Luciferase reporter assays for knockout verification**

609 For p53 activity measurement, 1 x 10<sup>6</sup> cells of control (WT) and clonally isolated p53 KO  
610 cell lines were electroporated with 3 µg p53 firefly luciferase reporter plasmid pp53-TA-  
611 Luc (Clontech/Takara) and 0.3 ug renilla luciferase control plasmid pRL-CMV  
612 (Promega) on an Amaxa Nucleofector 2b (Lonza). 24h later, cells were treated with 200  
613 uM etoposide (Sigma) to induce p53 activity. 24h following etoposide treatment, cells  
614 were harvested and luciferase activity of cell lysates was measured using the Dual-  
615 Luciferase Reporter Assay System (Promega) in a GloMax 20/20 Luminometer  
616 (Promega) according to manufacturer instructions.

617 For Rb activity measurement, 2 different reporters were tested in parallel: pE2F-TA-Luc  
618 (Clontech/Takara) to measure E2F transcriptional activity (repressed by Rb), and pRb-  
619 TA-Luc (Clontech/Takara) (promoter element directly suppressed by Rb). 1 x 10<sup>6</sup> cells  
620 of control (WT) and clonally isolated Rb KO cell lines were electroporated with 3 µg of  
621 either pE2F-TA-luc or pRb-TA-luc and 0.3 ug renilla luciferase plasmid on an Amaxa  
622 Nucleofector 2b (Lonza). Following transfection, cells were grown in complete medium

623 for 24h followed by serum-free medium for 24h. Cells were then harvested and  
624 luciferase activity measured as described above.

625 **Next-generation sequencing of CRISPR repair products**

626 72h after transfection, cells were harvested and genomic DNA was isolated with the  
627 Wizard Genomic DNA Purification Kit (Promega). DNA concentration was measured on  
628 a Nanodrop spectrophotometer and 100 ng of DNA per sample was PCR-amplified with  
629 KAPA2G Robust HotStart ReadyMix (Roche) based on findings of low PCR bias for  
630 KAPA polymerase<sup>9394</sup>. Primers targeted a conserved region surrounding *PTEN* exon 1  
631 (Extended Data Figure 4a). PCR was performed according to manufacturer instructions,  
632 with an annealing temperature of 66°C for 30 cycles. To purify samples for next-  
633 generation sequencing, PCR products were electrophoresed on a 0.8% agarose gel  
634 and post-stained with SYBR Gold Nucleic Acid Gel Stain (Thermo Fisher). Gels were  
635 visualized on a blue light tray (BioRad) to minimize damage to DNA. A gel slice for each  
636 lane was excised using a scalpel, and each slice was cut to include the region ranging  
637 from just above the prominent *PTEN* PCR band down to and including the “primer  
638 dimer” region to ensure inclusion of any deletion alleles. DNA was extracted from gel  
639 slices using the QiaQuick Gel Extraction Kit (Qiagen), and triplicate PCR reaction  
640 eluates per sample were pooled for sequencing. Sample concentrations were measured  
641 by Nanodrop and adjusted as necessary prior to submission for 2x250 bp paired-end  
642 Illumina MiSeq sequencing with target depth of >40,000 reads/sample (Genewiz).

643 **Analysis of CRISPR NGS data**

644 FASTQ files from each sequenced sample were analyzed with both CRISPResso2,<sup>95</sup>  
645 which uses an alignment-based algorithm, and CRISPRPic,<sup>96</sup> which uses a kmer-based  
646 algorithm. CRISPResso2 was run using the following parameters: window size = 30,  
647 maximum paired-end overlap = 500, bp excluded from left and right ends = 15,  
648 minimum alignment score = 50, minimum identity score = 50, plot window size = 20. For  
649 CRISPRPic analysis, SeqPrep<sup>97</sup> was used to merge overlapping read pairs and trim  
650 adapter sequences. CRISPRPic was run on merged FASTQ sequences for each  
651 sample with the following parameters: index size = 8, window size = 30.

652 **HPRT mutation assay**

653 For the HPRT mutation assay, cells used were low-passage primary dermal fibroblasts  
654 from multiple species that were known to originate from male animals, to ensure single  
655 copy-number of the X-linked *HPRT* gene. Each species was tested with 3 different cell  
656 lines from 3 individual animals. The bowhead *HPRT* coding sequence was BLASTed  
657 against bowhead genome scaffolds<sup>16</sup> and neighboring gene sequences were analyzed  
658 to confirm mammal-typical localization of *HPRT* on the bowhead X-chromosome. Cells  
659 were cultured in standard fibroblast growth medium, but with FBS being replaced with  
660 dialyzed FBS (Omega Scientific, Inc.) and supplemented with Fibroblast Growth Kit  
661 Serum-Free (Lonza) to improve growth and viability in dialyzed FBS. Dialyzed FBS was  
662 found in optimization experiments to be necessary for efficient 6-thioguanine selection.  
663 Prior to mutagenesis, cells were cultured for 7 days in medium containing HAT  
664 Supplement (Gibco) followed by 4 days in HT Supplement (Gibco) to eliminate any pre-  
665 existing HPRT mutants. To induce mutation, cells were incubated for 3 hours in serum-  
666 free MEM containing 150 µg/mL N-ethyl-N-nitrosourea (ENU) (Sigma). Cells were then

667 maintained in ENU-free medium for 9 days to allow mutations to establish and existing  
668 HPRT to degrade.  $1 \times 10^6$  cells from each cell line were harvested and plated in  
669 dialyzed FBS medium containing 5 µg/mL 6-thioguanine (Chem-Impex), in parallel with  
670  $1 \times 10^6$  untreated control cells for each cell line. Cells were plated at a density of  $1 \times 10^5$   
671 cells per 15-cm dish to allow for efficient selection and colony separation, and to prevent  
672 potential "metabolic cooperation"<sup>37</sup>. In tandem, for each cell line 200 cells from  
673 untreated and control conditions were plated in triplicate 10-cm dishes in non-selective  
674 medium to calculate plating efficiency. After 3 weeks of growth, surviving colonies were  
675 fixed and stained with a crystal violet/glutaraldehyde solution as previously described<sup>98</sup>.  
676 Colonies were counted, and HPRT mutation rate was calculated as plating-efficiency  
677 adjusted number of HPRT-negative colonies containing >50 cells. Appropriate  
678 concentrations of ENU and 6-TG, as well as optimal plating densities and growth  
679 conditions, were determined prior to the experiment described above through  
680 optimization and dose titration experiments.

#### 681 **Digital droplet PCR measurement of CRISPR cleavage rate**

682 A ddPCR assay similar to a previously published method<sup>99</sup> was used for time-course  
683 quantification of CRISPR DSB induction across species. qPCR primers at conserved  
684 sites flanking the guide RNA target site in the *PTEN* gene were designed such that  
685 cleavage would prevent PCR amplification. As an internal copy number reference  
686 control, a second set of previously validated qPCR primers targeting an ultraconserved  
687 element present in all mammals as a single copy per genome (UCE.359) was designed  
688 based on published sequences<sup>100</sup>. To allow for multiplexing and copy number  
689 normalization of *PTEN* within each ddPCR reaction, 5' fluorescent hydrolysis probes

690 (FAM for *PTEN* and HEX for UCE.359) targeting conserved sequences were designed,  
691 with 3' Iowa Black® and internal ZEN™ quenchers (Integrated DNA Technologies). All  
692 primers and probes were checked for specificity by BLAST against each species'  
693 genome.<sup>100</sup> Fibroblasts were transfected with *PTEN* CRISPR RNP as described in  
694 "Next-generation sequencing of CRISPR repair products" and returned to cell culture  
695 incubators. At the indicated times post-transfection, cells were harvested, flash frozen,  
696 and genomic DNA was isolated with the Wizard Genomic DNA Purification Kit  
697 (Promega). During isolation, newly lysed cells were treated with Proteinase K and  
698 RNase A for 30 minutes each at 37°C to minimize the possibility of residual CRISPR  
699 RNP activity. DNA concentration was measured on a Nanodrop spectrophotometer, and  
700 genomic DNA was pre-digested with BamHI-HF (NEB) and Xhol (NEB), which do not  
701 cut within target amplicons, to maximize PCR efficiency and distribution across droplets.  
702 15 ng of genomic DNA per sample was added to duplicate PCR reactions using the  
703 ddPCR™ Supermix for Probes (No dUTP) master mix (Bio-Rad). Droplets were  
704 prepared and measured according to manufacturer instructions. Briefly, each 20 µL  
705 reaction was mixed with 70 µL Droplet Generation Oil for Probes (Bio-Rad) and droplets  
706 were formed in a QX100 Droplet Generator (Bio-Rad). 40 µL of droplets per reaction  
707 were transferred to 96-well PCR plates and sealed with a PX1 PCR Plate Sealer (Bio-  
708 Rad). The sealed plates were then subjected to PCR using a pre-optimized cycling  
709 protocol. Following PCR, the plates were loaded into a QX100™ Droplet Reader (Bio-  
710 Rad) and each droplet measured on both FAM and HEX channels. *PTEN* copy number  
711 normalized to UCE.359 reference copy number within each well was determined with  
712 QuantaSoft™ software (Bio-Rad). For each species, positive/negative gates in mock-

713 transfected control samples were adjusted as necessary to compensate for differences  
714 in multiplex PCR efficiency/specificity and “rain” droplets between species and bring  
715 normalized *PTEN* copy number closer to 1. The control gates were then applied across  
716 all samples/time points within the same species and used for *PTEN* copy number  
717 calculation.

718 **Flow cytometric measurement of CRISPR RNP transfection efficiency**

719 CRISPR RNP transfections were performed as described above, but with ATTO-550  
720 fluorescently-labeled tracRNA (Integrated DNA Technologies). At 0h and 24h post-  
721 transfection, cells were harvested, pelleted, and analyzed by flow cytometry on a  
722 CytoFlex S Flow Cytometer (Beckman Coulter). Gain and ATTO-550 positive gates  
723 were set based on mock-transfected control cells included in each experiment.

724 **Senescence-associated β-galactosidase (SA-β-gal) staining**

725 SA-β-gal staining was performed as previously described.<sup>101,102</sup> Cells were washed  
726 twice with PBS and fixed in a solution containing 2% formaldehyde and 0.2%  
727 glutaraldehyde in PBS for 5 min at room temperature. After fixation, cells were  
728 immediately washed twice with PBS and stained in a solution containing 1 mg/mL 5-  
729 bromo-4-chloro-3-indolyl P3-D-galactoside (X-Gal), 40 mM citric acid/sodium phosphate  
730 buffer, pH 6.0, 5 mM potassium ferrocyanide, 5 mM potassium ferricyanide, 150 mM  
731 NaCl, and 2 mM MgCl<sub>2</sub>. Plates were incubated at 37°C for 16 h without CO<sub>2</sub>.  
732 Colorimetric images were taken from different areas of each plate and quantified.

733 **Cell survival assay**

734 Percentage of live cells was quantified using the Annexin-V FLUOS Staining Kit (Roche)  
735 following the manufacturer's instructions. After staining, cells were analyzed on a  
736 CytoFlex S flow cytometer (Beckman Coulter).

737 **p53 activity**

738 To test p53 activity in cultured primary fibroblasts, 150,000 cells were seeded in 6-well  
739 plates 1 day before transfection with 1 µg pp53-TA-Luc vector (Clontech) and 0.015 µg  
740 pRL-CMV-Renilla (Promega) to normalize for transfection efficiency. Transfections were  
741 performed using PEI MAX Transfection Grade Linear Polyethylenimine Hydrochloride  
742 (MW 40,000) (Polysciences) according to manufacturer instructions. 24h after  
743 transfections cells were lysed using 50µl passive lysis buffer (Promega) per  $10^5$  cells  
744 and flash frozen/thawed two times in liquid nitrogen and a 37°C water bath. Luciferase  
745 assays were performed using the Dual-Luciferase Reporter Assay System (Promega)  
746 and program DLR-2-INJ on a Glomax 20/20 Luminometer (Promega) with 20µl cell  
747 extract as the input.

748 **Generation of NHEJ and HR reporter cell lines**

749 NHEJ and HR reporter constructs<sup>38</sup> were digested with NheI restriction enzyme and  
750 purified with the QIAEX II gel extraction kit (QIAGEN). The same plasmid DNA  
751 preparation was used for generating all reporter cell lines of the studied species. Cells  
752 PD < 15 were recovered from liquid nitrogen and passaged once before the integration  
753 of the constructs. 0.25 µg of linearized NHEJ and HR constructs were electroporated  
754 into one million cells for each cell line. Two days after transfection, media was  
755 refreshed, and G418 was applied to select stable integrant clones. Triplicates of each

756 reporter in each cell line were prepared to obtain an adequate number of stable clones.  
757 Clones from triplicate plates were pooled to get at least 50 clones per reporter per cell  
758 line.

### 759 **DSB repair assays and flow cytometry analysis**

760 DSB repair assays were performed as previously described<sup>103</sup>. Briefly, growing cells  
761 were co-transfected with 3 µg of plasmid encoding I-SceI endonuclease and 0.03 µg of  
762 plasmid encoding DsRed. The same batch of I-SceI and DsRed mixture was used  
763 throughout all species to avoid batch-to-batch variation. To test the effect of CIRBP on  
764 DSB repair, 3 µg of CIRBP plasmids were co-transfected with I-SceI and DsRed  
765 plasmids. Three days after transfection, the numbers of GFP+ and DsRed+ cells were  
766 determined by flow cytometry on a CytoFlex S Flow Cytometer (Beckman Coulter). For  
767 gating strategy see Supplementary Figure 4 in Supplementary Information. For each  
768 sample, a minimum of 50,000 cells was analyzed. DSB repair efficiency was calculated  
769 by dividing the number of GFP+ cells by the number of DsRed+ cells.

770 For knockdown experiments, bowhead whale cells containing the NHEJ reporter were  
771 transfected with 120 pmol of anti-bwCIRBP or control siRNAs (Dharmacon) 3 days  
772 before I-Sce1/DsRed transfections using an Amaxa Nucleofector (U-023 program). The  
773 efficiency of knockdown was determined by Western blot.

774 For the extrachromosomal assay and fidelity analysis, NHEJ reporter plasmid was  
775 digested with I-Sce1 for 6h and purified using a QIAEX II Gel Extraction Kit (QIAGEN).  
776 Exponentially growing cells were transfected using an Amaxa nucleofector with the U-  
777 023 program. In a typical reaction, 10<sup>6</sup> cells were transfected with 0.25 µg of

778 predigested NHEJ reporter substrate along with 0.025 µg of DsRed to serve as a  
779 transfection control. 72h after transfection, cells were harvested and analyzed by flow  
780 cytometry on a BD LSR II instrument. At least 20,000 cells were collected for each  
781 sample. Immediately after FACS, genomic DNA was isolated from cells using the  
782 QIAGEN Blood & Tissue kit. DSB repair sites in the NHEJ construct were amplified by  
783 PCR using Phusion polymerase (NEB), cloned using the TOPO Blunt cloning kit (NEB),  
784 and sent for Sanger sequencing. At least 100 sequenced clones were aligned and  
785 analyzed using the ApE software.

786 **Western blotting**

787 All antibodies were checked for conservation of the target epitope in the protein  
788 sequence of each included species, and only those targeting regions conserved across  
789 these species were used. For a limited number of proteins where the available  
790 antibodies with specific epitope information disclosed did not target conserved regions,  
791 we selected antibodies based on demonstrated reactivity across a broad range of  
792 mammal species and always confirmed these results with multiple antibodies.  
793 Information on antibodies is provided in Supplementary Methods.

794 Exponentially growing cells were harvested with trypsin and counted, and  $10^6$  cells were  
795 resuspended in 100 µL of PBS containing protease inhibitors. 100µL of 2x Laemmli  
796 buffer (Bio-Rad) was added, and samples were boiled at 95°C for 10 minutes. Samples  
797 were separated with 4-20% gradient SDS-PAGE, transferred to a PVDF membrane,  
798 and blocked in 5% milk-TBS-T for 2 hours at room temperature. Membranes were  
799 incubated overnight at +4°C with primary antibodies in 5% milk-TBS-T. After 3 washes  
800 for 10 minutes with TBS-T, membranes were incubated for 1 hour at room temperature

801 with secondary antibodies conjugated with HRP or a fluorophore. After 3 washes with  
802 TBS-T signal was developed for HRP secondaries with Clarity Western ECL Substrate  
803 (Bio-Rad). CIRBP and RPA2 expression were each measured with 3 different  
804 antibodies targeting conserved epitopes (Extended Data Figure 7c, d).

805 **PARP activity**

806 PARP activity was measured in cell nuclear extracts with the PARP Universal  
807 Colorimetric Assay Kit (Trevigen) according to the manufacturer's instructions. Nuclear  
808 extracts were prepared using EpiQuik Nuclear Extraction Kit (EpigenTek) following  
809 manufacturer protocol. 2.5 $\mu$ g of total nuclear extract was added to measure PARP  
810 activity.

811 For measurement of PARylation efficiency, cells were treated with 400 $\mu$ M H<sub>2</sub>O<sub>2</sub> for 15  
812 and 30 min. At the end of incubation, cells were placed on ice, washed once with PBS,  
813 and lysed directly on a plate with 2x Laemmli buffer. Samples were boiled for 10min at  
814 95°C and processed by Western Blot.

815 **Pulsed-field gel electrophoresis and analysis of DSBs**

816 After irradiation and repair incubation, confluent human and bowhead whale skin  
817 fibroblasts were harvested, ~400,000 cells were resuspended in PBS, mixed with an  
818 equal volume of 1.4% low gelling temperature agarose and embedded into agarose  
819 plugs. Plugs were kept for 1h at +4°C and incubated in lysis solution 1 (0.5M EDTA, 2%  
820 sodium sarcosine, 0.5 mg/ml Proteinase K) for 24h at +4°C. Subsequently plugs were  
821 placed into lysis solution 2 (1.85M NaCl, 0.15M KCl, 5mM MgCl<sub>2</sub>, 2mM EDTA, 4mM Tris  
822 pH 7.5, 0.5% TritonX100) for 40h at +4°C. Plugs were then washed two times for 1h in

823 TE buffer and stored in TE buffer at +4°C. PFGE was carried out with a CHEF DRII  
824 system (Bio-Rad) in 0.8% agarose gels. The gels were run at 14°C with linearly  
825 increasing pulse times from 50 to 5,000 s for 66 h at a field strength of 1.5 V/cm. Gels  
826 were stained with 0.5mg/ml ethidium bromide for 4h, washed with TBE buffer and  
827 imaged. Quantitative analysis was performed with Image Lab software (Bio-Rad). The  
828 fraction of DNA entering the gel was quantified. Samples irradiated with various doses  
829 and not incubated for repair served as a calibration to determine the percentage of  
830 remaining DSBs in the repair samples from the fraction of DNA entering the gel.

831 **Construction of lentiviral overexpression vectors and lentivirus production**

832 The coding sequence of bwCIRBP was amplified by PCR using Phusion polymerase  
833 (NEB), digested with EcoRI and NotI, and cloned in between EcoRI and NotI sites of the  
834 Lego-iC2 plasmid. The sequence was verified by Sanger sequencing.

835 Lentiviral particles were produced in Lenti-X 293T cells (Takara). Approximately 10x10<sup>6</sup>  
836 cells were transfected with a mixture of pVSV-G (1.7 µg), psPAX2 (3.4 µg) and Lego-  
837 iC2-bwCIRBP (6.8 µg) using PEI MAX (Polysciences). The day after transfection,  
838 DMEM culture medium (ThermoFisher) was replaced with fresh medium and lentiviral  
839 particles were harvested from the supernatant for the next 3 days.

840 **Quantification of micronuclei**

841 Two different approaches were used. To analyze binucleated cells containing  
842 micronuclei (MN), 20,000 cells were plated per chamber slide 2d before ionizing  
843 radiation. Immediately after irradiation (for human cells) or 2d after irradiation (for  
844 bowhead whale cells), cytochalasin B was added to cell culture media at a final

845 concentration 0.5 µg/ml, and cells were incubated for an additional 72h. At the end of  
846 incubation, cells were washed with PBS, incubated in 75mM KCl for 10min at RT, fixed  
847 with ice-cold methanol for 1.5 min, air-dried, and stored. Immediately before the  
848 analysis, cells were stained with 100 µg/ml acridine orange for 2min, washed with PBS,  
849 mounted in PBS and analyzed by fluorescence microscopy. At least 1000 binucleated  
850 cells were analyzed per sample.

851 For analysis of MN in single cells overexpressing bwCIRBP, exponentially growing cells  
852 were transduced with LEGO-iC2-bwCIRBP lentivirus in the presence of 10 µg/ml  
853 polybrene. Two days after transduction, cells were passaged, and irradiated the  
854 following day. 3 days after irradiation, cells were fixed with 2% formaldehyde for 15 min,  
855 washed with PBS, permeabilized with 0.2% TritonX100 for 2min, washed in PBS, and  
856 mounted in VECTASHIELD Antifade Mounting Medium with DAPI. Cells were analyzed  
857 with a fluorescent microscope. At least 1000 cells were analyzed per condition.

### 858 **Host cell reactivation assay**

859 A host cell reactivation assay was used to measure the repair of UV-induced DNA  
860 damage through nucleotide excision repair as previously described.<sup>33</sup>

861 To measure the repair of oxidative DNA damage (base excision repair), 20 µg of firefly  
862 luciferase (FFL) plasmid was mixed with 20-200 µM methylene blue (MB), and water  
863 was added to a final volume of 0.4ml. DNA-MB mixture was dropped onto a petri dish  
864 and placed on ice. An additional petri dish containing water was placed on top. The  
865 DNA-MB mixture was exposed to visible light for 15 min using a 100W lamp at an 11cm

866 distance. Damaged DNA was purified, and the host cell reactivation assay was  
867 performed as described for UV-induced DNA damage.

868 **Cyclobutane pyrimidine dimer (CPD) ELISA**

869 Human and bowhead whale skin fibroblasts were grown until they reached confluence  
870 before UVC radiation. Cells were irradiated in PBS at doses of 0, 5, 10, 20 and 30J/m<sup>2</sup>  
871 and harvested immediately for building an induction curve. To assess DNA repair, cells  
872 were irradiated at 30 J/m<sup>2</sup> and incubated for 6, 24 and 48h before harvesting. Genomic  
873 DNA was isolated using QIAamp Blood Kit (Qiagen). Samples of DNA were diluted in  
874 PBS to a final concentration of 2 µg/ml, denatured at 100°C for 10min and incubated in  
875 an ice bath for 15 min. 100 ng of denatured DNA solution was applied to ELISA plate  
876 wells precoated with protamine sulfate (Cosmo Bio) and dried O/N at 37°C. Plates were  
877 washed five times with PBS supplemented with 0.05% Tween-20 (PBS-T) and blocked  
878 in 2% FBS in PBS-T for 30min at 37°C. After 5 washes with PBS-T, plates were  
879 incubated with mouse monoclonal anti-CPD antibodies (Clone TDM-2, 1:1000) in PBS  
880 for 30 min at 37°C. Plates were then sequentially incubated with goat-anti mouse biotin  
881 IgG (Invitrogen, 1:1000) and streptavidin-HRP (Invitrogen, 1:5000) in PBS for 30 min at  
882 37°C each with 5 washes with PBS-T before and after incubations. Plates were washed  
883 with citrate buffer and incubated with substrate solution (citrate buffer/o-  
884 phenylenediamine/hydrogen peroxide) for 30 min at 37°C. Finally, the reaction was  
885 stopped with 2M H<sub>2</sub>SO<sub>4</sub> and the absorbance was measured at 492 nm with a plate  
886 reader.

887 **CIRBP variant sequence analysis**

888 Identification of rare codons (<10% usage for the corresponding amino acid in human  
889 CDS sequences) was performed on CIRBP coding sequences using the Benchling  
890 Codon Optimization Tool.<sup>104</sup> Codon adaptation index (CAI) was calculated with human  
891 codon frequencies using the E-CAI web server.<sup>53</sup>

892 **RNA isolation and RNA-seq analysis**

893 RNA from exponentially growing or senescent human and bowhead whale primary skin  
894 fibroblasts was isolated using the Quick-RNA MiniPrep kit (Zymo Research) according  
895 to manufacturer instructions.

896 The RNA-seq reads were first processed using Trim\_Galore (version 0.6.6). Cleaned  
897 RNA-seq reads were used to quantify gene expression with Salmon (version 1.4.0).<sup>105</sup>  
898 Transcript FASTA files of species were from our published de novo transcriptome  
899 assemblies.<sup>106</sup> Transcript FASTA files were indexed with the command “Salmon index”  
900 with default parameters. Cleaned RNA-seq reads were aligned to the indexed transcript  
901 with the specific parameters (--useVBOpt --seqBias --gcBias), which were set for  
902 sequence-specific bias correction and fragment GC bias correction. The read counts of  
903 genes obtained from Salmon were further normalized by trimmed mean of M-values  
904 (TMM)<sup>107</sup> and median of ratios methods.<sup>108</sup>

905 **LC-MS proteomic analysis of fibroblasts**

906 2 15-cm dishes of growing primary fibroblasts from 2 cell lines for each species were  
907 harvested for protein. Cells were washed with PBS and pellets were snap frozen and  
908 stored in liquid nitrogen until processing. Cells were solubilized with 5% SDS; 50 mM  
909 TEAB pH 7, and sonicated at 8°C with 10x 45s pulses using 30% power with 15 s rest

910 between each pulse with a cup horn Q800R3 Sonicator System (Qsonica; Newtown  
911 CT). Soluble proteins were reduced with 10 mM DTT for 30 min at 55°C, followed by  
912 alkylation with 15 mM iodoacetamide at 25°C in the dark for 30 min. S-trap micro  
913 columns (Protifi; Farmingdale, NY) were employed after this step for overnight tryptic  
914 digestion and peptide isolation according to manufacturer instructions. All solvents were  
915 MS-grade. Resulting tryptic peptides were resuspended in MS-grade water and were  
916 quantified using a Pierce™ Quantitative Fluorometric Peptide Assay (Thermo Fisher cat  
917 #23290). Prior to MS, peptides were mixed with a common internal retention time  
918 standards<sup>109</sup> (CiRT) peptide mix (50 fmol CiRT/2ug total tryptic peptides) and  
919 acetonitrile (ACN) and formic acid were added to concentrations of 5% and 0.2%  
920 respectively. The final concentration of the peptide mix was 0.5µg/µl. 2ug (4ul) of each  
921 were resolved by nano-electrospray ionization on an Orbitrap Fusion Lumos MS  
922 instrument (Thermo) in positive ion mode. A 30 cm home-made column packed with 1.8  
923 µm C-18 beads was employed to resolve the peptides. Solvent A was 0.1% formic acid  
924 and solvent B was 80% acetonitrile with 0.1% formic acid and flow rate was 300 nl/min.  
925 The length of the run was 3 h with a 155 min gradient from 10-38% B. HCD (30%  
926 collision energy) was used for MS2 fragmentation and dynamic exclusion was operative  
927 after a single time and lasted for 30s. Other details of the run parameters may be found  
928 in the embedded run report of the RAW data file uploaded to the ProteomeXchange  
929 database. Peptide assignments and quantitation were done using the label-free quant  
930 match between runs (LFQ-MBR) workflow of MSFragger<sup>110–112</sup>. MaxLFQ with a  
931 minimum of two ions was implemented and normalization was selected. Additional  
932 details are available in MSFragger log files. Searches were performed within the

933 Philosopher/Fragpipe pipeline that incorporates PeptideProphet and ProteinProphet  
934 filtering steps to increase the likelihood of correct assignments.<sup>113</sup> The databases used  
935 for searches were predicted proteins from the published bowhead genome<sup>114</sup> as well as  
936 our custom proteome derived from our de novo sequenced and Trinity<sup>115,116</sup>-assembled  
937 pool of transcriptomes from whale tissues. Human (UP000005640), mouse  
938 (UP000000589), and bovine (UP000009136) databases were from the latest build  
939 available from Uniprot.<sup>117</sup> For the searches, databases also included a reverse  
940 complement form of all peptides as well as common contaminants to serve as decoys  
941 for false discovery rate (FDR) calculation by the target/decoy approach (decoy present  
942 at 50%).<sup>118</sup> Final FDR was below 1%.

#### 943 **Statistical analyses**

944 Statistical comparisons were performed as indicated in the figure legends. Unless  
945 otherwise specified in the text or legend, *n* refers to separate biological replicate cell  
946 lines, isolated from different individuals for a given species. Exceptions include specific  
947 genetically modified cell lines or clones, e.g. tumor suppressor knockout lines and Ku-  
948 deficient MEFs. In such cases, *n* refers to technical replicates and indicates the number  
949 of times the experiment was repeated with the specified cell line. Details for  
950 comparisons done by ANOVA are included in Supplementary Information.

#### 951 **Data Availability**

952 Proteomics data are accessible through ProteomeXchange [URL to be added]. DNA  
953 sequence (CRISPR repair fidelity analysis) and RNA sequence (transcriptome) data are  
954 accessible through NCBI Sequence Read Archive (SRA) [URL to be added].

## 955 References

- 956 1. Tacutu, R. *et al.* Human Ageing Genomic Resources: new and updated databases. *Nucleic Acids*  
957 *Res* **46**, D1083–D1090 (2018).
- 958 2. Peto, R. Epidemiology, multistage models, and short-term mutagenicity tests. in *The origins of*  
959 *human cancer* (eds. Hiatt, H., Watson, J. & Winsten, J.) vol. 4 1403–1428 (Cold Spring Harbor  
960 Conferences on Cell Proliferation, 1977).
- 961 3. Abegglen, L. M. *et al.* Potential Mechanisms for Cancer Resistance in Elephants and Comparative  
962 Cellular Response to DNA Damage in Humans. *JAMA* **314**, 1850 (2015).
- 963 4. Vazquez, J. M., Sulak, M., Chigurupati, S. & Lynch, V. J. A Zombie LIF Gene in Elephants Is  
964 Upregulated by TP53 to Induce Apoptosis in Response to DNA Damage. *Cell Rep* **24**, 1765–1776  
965 (2018).
- 966 5. Sulak, M. *et al.* TP53 copy number expansion is associated with the evolution of increased body  
967 size and an enhanced DNA damage response in elephants. *Elife* **5**, (2016).
- 968 6. TEK & Bowhead Life History and Longevity - The North Slope Borough. <https://www.north-slope.org/departments/wildlife-management/studies-research-projects/bowhead-whales/traditional-ecological-knowledge-of-bowhead-whales/tek-bowhead-life-history-and-longevity/>.
- 972 7. George, J. C. & Bockstoce, J. R. Two historical weapon fragments as an aid to estimating the  
973 longevity and movements of bowhead whales. *Polar Biol* **31**, 751–754 (2008).
- 974 8. Rosa, C. *et al.* Age estimates based on aspartic acid racemization for bowhead whales (*Balaena*  
975 *mysticetus*) harvested in 1998–2000 and the relationship between racemization rate and body  
976 temperature. *Mar Mamm Sci* **29**, 424–445 (2013).
- 977 9. Philo, L. M., Shotts, E. B. & George, J. C. Morbidity and mortality- The bowhead whale. *Soc. Mar.*  
978 *Mammal., Spec. Publ* 275–312 (1993).
- 979 10. George, J. C. *et al.* Age and growth estimates of bowhead whales (*Balaena mysticetus*) via  
980 aspartic acid racemization. *Can J Zool* **77**, 571–580 (1999).
- 981 11. Wetzel, D. *et al.* Age estimation for bowhead whales, *Balaena mysticetus*, using aspartic acid  
982 racemization with enhanced hydrolysis and derivatization procedures. *Paper SC/65b/BRG05*  
983 *presented to the Scientific Committee of the International Whaling Commission* (2014).
- 984 12. George, J. C. *et al.* A new way to estimate the age of bowhead whales (*Balaena mysticetus*) using  
985 ovarian corpora counts. <https://doi.org/10.1139/z11-057> **89**, 840–852 (2011).
- 986 13. Boddy, A. M. *et al.* Lifetime cancer prevalence and life history traits in mammals. *Evol Med Public*  
987 *Health* **2020**, 187–195 (2020).
- 988 14. Vincze, O. *et al.* Cancer risk across mammals. *Nature* **601**, 263–267 (2022).
- 989 15. Tollis, M., Boddy, A. M. & Maley, C. C. Peto's Paradox: how has evolution solved the problem of  
990 cancer prevention? *BMC Biol* **15**, (2017).

- 991 16. Keane, M. *et al.* Insights into the evolution of longevity from the bowhead whale genome. *Cell Rep* **10**, 112–122 (2015).
- 993 17. Tollis, M. *et al.* Return to the Sea, Get Huge, Beat Cancer: An Analysis of Cetacean Genomes  
994 Including an Assembly for the Humpback Whale (*Megaptera novaeangliae*). *Mol Biol Evol* **36**,  
995 1746–1763 (2019).
- 996 18. Seim, I. *et al.* The transcriptome of the bowhead whale *Balaena mysticetus* reveals adaptations of  
997 the longest-lived mammal. *Aging* **6**, 879–899 (2014).
- 998 19. Armitage, P. & Doll, R. The age distribution of cancer and a multi-stage theory of carcinogenesis.  
999 *Br J Cancer* **8**, 1–12 (1954).
- 1000 20. Rangarajan, A., Hong, S. J., Gifford, A. & Weinberg, R. A. Species- and cell type-specific  
1001 requirements for cellular transformation. *Cancer Cell* **6**, 171–183 (2004).
- 1002 21. Vazquez, J. M., Sulak, M., Chigurupati, S. & Lynch, V. J. A Zombie LIF Gene in Elephants Is  
1003 Upregulated by TP53 to Induce Apoptosis in Response to DNA Damage. *Cell Rep* **24**, 1765–1776  
1004 (2018).
- 1005 22. Vazquez, J. M. & Lynch, V. J. Pervasive duplication of tumor suppressors in Afrotherians during  
1006 the evolution of large bodies and reduced cancer risk. *Elife* **10**, 1–45 (2021).
- 1007 23. Vazquez, J. M. *et al.* Parallel evolution of reduced cancer risk and tumor suppressor duplications  
1008 in Xenarthra. *Elife* **11**, (2022).
- 1009 24. Boveri, T. Concerning the origin of malignant tumours by Theodor Boveri. Translated and  
1010 annotated by Henry Harris. *J Cell Sci* **121**, 1–84 (2008).
- 1011 25. Hasty, P., Campisi, J., Hoeijmakers, J., van Steeg, H. & Vijg, J. *Aging and Genome Maintenance:  
1012 Lessons from the Mouse?* <http://science.sciencemag.org/>.
- 1013 26. Kashiyama, K. *et al.* Malfunction of nuclease ERCC1-XPF results in diverse clinical manifestations  
1014 and causes Cockayne syndrome, xeroderma pigmentosum, and Fanconi anemia. *Am J Hum Genet*  
1015 **92**, 807–819 (2013).
- 1016 27. Navarro, C. L., Cau, P. & Lévy, N. Molecular bases of progeroid syndromes. *Human Molecular  
1017 Genetics* vol. 15 R151–R161 Preprint at <https://doi.org/10.1093/hmg/ddl214> (2006).
- 1018 28. Varon, R. *et al.* Nibrin, a novel DNA double-strand break repair protein, is mutated in Nijmegen  
1019 breakage syndrome. *Cell* **93**, 467–476 (1998).
- 1020 29. Liu, B. *et al.* Genomic instability in laminopathy-based premature aging. *Nat Med* **11**, 780–785  
1021 (2005).
- 1022 30. Lorenzini, A. *et al.* Significant Correlation of Species Longevity with DNA Double Strand Break-  
1023 Recognition but not with Telomere Length. *Mech Ageing Dev* **130**, 784 (2009).
- 1024 31. Zhang, L. *et al.* Maintenance of genome sequence integrity in long- And short-lived rodent  
1025 species. *Sci Adv* **7**, (2021).

- 1026 32. Cagan, A. *et al.* Somatic mutation rates scale with lifespan across mammals. *Nature* 2022 1–8  
1027 (2022) doi:10.1038/s41586-022-04618-z.
- 1028 33. Tian, X. *et al.* SIRT6 Is Responsible for More Efficient DNA Double-Strand Break Repair in Long-  
1029 Lived Species. *Cell* 177, 622–638.e22 (2019).
- 1030 34. Fortunato, A., Fleming, A., Aktipis, A. & Maley, C. C. Upregulation of DNA repair genes and cell  
1031 extrusion underpin the remarkable radiation resistance of *Trichoplax adhaerens*. *PLoS Biol* 19,  
1032 (2021).
- 1033 35. Tian, X. *et al.* Evolution of telomere maintenance and tumour suppressor mechanisms across  
1034 mammals. *Philosophical Transactions of the Royal Society B: Biological Sciences* 373, (2018).
- 1035 36. Borowicz, S. *et al.* The soft agar colony formation assay. *J Vis Exp* e51998 (2014)  
1036 doi:10.3791/51998.
- 1037 37. Johnson, G. E. Mammalian Cell HPRT Gene Mutation Assay: Test Methods. in 55–67 (2012).  
1038 doi:10.1007/978-1-61779-421-6\_4.
- 1039 38. Seluanov, A., Mao, Z. & Gorbunova, V. Analysis of DNA Double-strand Break (DSB) Repair in  
1040 Mammalian Cells. *J Vis Exp* 43 (2010) doi:10.3791/2002.
- 1041 39. Guo, T. *et al.* Harnessing accurate non-homologous end joining for efficient precise deletion in  
1042 CRISPR/Cas9-mediated genome editing. *Genome Biol* 19, (2018).
- 1043 40. Richardson, C. D., Ray, G. J., Bray, N. L. & Corn, J. E. Non-homologous DNA increases gene  
1044 disruption efficiency by altering DNA repair outcomes. *Nature Communications* 2016 7:1 7, 1–7  
1045 (2016).
- 1046 41. Chen, J. K., Lin, W. L., Chen, Z. & Liu, H. wen. PARP-1-dependent recruitment of cold-inducible  
1047 RNA-binding protein promotes double-strand break repair and genome stability. *Proc Natl Acad  
1048 Sci U S A* 115, E1759–E1768 (2018).
- 1049 42. Nishiyama, H. *et al.* A glycine-rich RNA-binding protein mediating cold-inducible suppression of  
1050 mammalian cell growth. *J Cell Biol* 137, 899–908 (1997).
- 1051 43. Sheikh, M. S. *et al.* Identification of several human homologs of hamster DNA damage-inducible  
1052 transcripts. Cloning and characterization of a novel UV-inducible cDNA that codes for a putative  
1053 RNA-binding protein. *J Biol Chem* 272, 26720–26726 (1997).
- 1054 44. Wellmann, S. *et al.* Oxygen-regulated expression of the RNA-binding proteins RBM3 and CIRP by  
1055 a HIF-1-independent mechanism. *J Cell Sci* 117, 1785–1794 (2004).
- 1056 45. Yang, C. & Carrier, F. The UV-inducible RNA-binding protein A18 (A18 hnRNP) plays a protective  
1057 role in the genotoxic stress response. *J Biol Chem* 276, 47277–47284 (2001).
- 1058 46. Yang, R., Weber, D. J. & Carrier, F. Post-transcriptional regulation of thioredoxin by the stress  
1059 inducible heterogenous ribonucleoprotein A18. *Nucleic Acids Res* 34, 1224–1236 (2006).

- 1060 47. Yang, R. *et al.* Functional significance for a heterogenous ribonucleoprotein A18 signature RNA  
1061 motif in the 3'-untranslated region of ataxia telangiectasia mutated and Rad3-related (ATR)  
1062 transcript. *J Biol Chem* **285**, 8887–8893 (2010).
- 1063 48. Roilo, M., Kullmann, M. K. & Hengst, L. Cold-inducible RNA-binding protein (CIRP) induces  
1064 translation of the cell-cycle inhibitor p27Kip1. *Nucleic Acids Res* **46**, 3198–3210 (2018).
- 1065 49. Elsner, R., Meiselman, H. J. & Baskurt, O. K. TEMPERATURE-VISCOSITY RELATIONS OF BOWHEAD  
1066 WHALE BLOOD: A POSSIBLE MECHANISM FOR MAINTAINING COLD BLOOD FLOW. *Mar Mamm Sci*  
1067 **20**, 339–344 (2004).
- 1068 50. George, J. C. Growth, morphology and energetics of bowhead whales (*Balaena mysticetus*).  
1069 (University of Alaska Fairbanks, 2009).
- 1070 51. Gotic, I. *et al.* Temperature regulates splicing efficiency of the cold-inducible RNA-binding protein  
1071 gene Cirbp. *Genes Dev* **30**, 2005–2017 (2016).
- 1072 52. Al-Fageeh, M. B. & Smales, C. M. Cold-inducible RNA binding protein (CIRP) expression is  
1073 modulated by alternative mRNAs. *RNA* **15**, 1165–1176 (2009).
- 1074 53. Puigbò, P., Bravo, I. G. & Garcia-Vallvé, S. E-CAI: a novel server to estimate an expected value of  
1075 Codon Adaptation Index (eCAI). *BMC Bioinformatics* **9**, (2008).
- 1076 54. Zou, Y., Liu, Y., Wu, X. & Shell, S. M. Functions of Human Replication Protein A (RPA): From DNA  
1077 Replication to DNA Damage and Stress Responses. *J Cell Physiol* **208**, 267 (2006).
- 1078 55. Wold, M. S. Replication protein A: a heterotrimeric, single-stranded DNA-binding protein  
1079 required for eukaryotic DNA metabolism. *Annu Rev Biochem* **66**, 61–92 (1997).
- 1080 56. Paulsen, R. D. *et al.* A genome-wide siRNA screen reveals diverse cellular processes and pathways  
1081 that mediate genome stability. *Mol Cell* **35**, 228–239 (2009).
- 1082 57. Toledo, L. I. *et al.* ATR prohibits replication catastrophe by preventing global exhaustion of RPA.  
1083 *Cell* **155**, 1088 (2013).
- 1084 58. Velegzhaninov, I. O. *et al.* Radioresistance, DNA Damage and DNA Repair in Cells With Moderate  
1085 Overexpression of RPA1. *Front Genet* **11**, 855 (2020).
- 1086 59. Guven, M., Brem, R., Macpherson, P., Peacock, M. & Karran, P. Oxidative damage to RPA limits  
1087 the nucleotide excision repair capacity of human cells. *J Invest Dermatol* **135**, 2834 (2015).
- 1088 60. Graziano, S. *et al.* Lamin A/C recruits ssDNA protective proteins RPA and RAD51 to stalled  
1089 replication forks to maintain fork stability. *Journal of Biological Chemistry* **297**, 101301 (2021).
- 1090 61. Perrault, R., Cheong, N., Wang, H., Wang, H. & Iliakis, G. RPA facilitates rejoining of DNA double-  
1091 strand breaks in an in vitro assay utilizing genomic DNA as substrate. *int. j. radiat. biol.* **77**, 593–  
1092 607 (2001).
- 1093 62. Krasner, D. S., Daley, J. M., Sung, P. & Niu, H. Interplay between Ku and Replication Protein A in  
1094 the Restriction of Exo1-mediated DNA Break End Resection. *J Biol Chem* **290**, 18806–18816  
1095 (2015).

- 1096 63. Chen, H., Lisby, M. & Symington, L. S. RPA coordinates DNA end resection and prevents  
1097 formation of DNA hairpins. *Mol Cell* **50**, 589–600 (2013).
- 1098 64. Deng, S. K., Gibb, B., de Almeida, M. J., Greene, E. C. & Symington, L. S. RPA Antagonizes  
1099 Microhomology-Mediated Repair of DNA Double-Strand Breaks. *Nat Struct Mol Biol* **21**, 405  
1100 (2014).
- 1101 65. Guven, M., Brem, R., Macpherson, P., Peacock, M. & Karran, P. Oxidative damage to RPA limits  
1102 the nucleotide excision repair capacity of human cells. *J Invest Dermatol* **135**, 2834 (2015).
- 1103 66. Kim, K. *et al.* Novel Checkpoint Response to Genotoxic Stress Mediated by Nucleolin-Replication  
1104 Protein A Complex Formation. *Mol Cell Biol* **25**, 2463 (2005).
- 1105 67. Bélanger, F. *et al.* Mutations in Replicative Stress Response Pathways Are Associated with S  
1106 Phase-specific Defects in Nucleotide Excision Repair \*. (2015) doi:10.1074/jbc.M115.685883.
- 1107 68. Shuck, S. C. & Turchi, J. J. Targeted inhibition of RPA reveals cytotoxic activity, synergy with  
1108 chemotherapeutic DNA damaging agents and insight into cellular function. *Cancer Res* **70**, 3189  
1109 (2010).
- 1110 69. White, R. R. *et al.* Double-Strand Break Repair by Interchromosomal Recombination: An In Vivo  
1111 Repair Mechanism Utilized by Multiple Somatic Tissues in Mammals. *PLoS One* **8**, 84379 (2013).
- 1112 70. Seluanov, A. *et al.* Telomerase activity coevolves with body mass not lifespan. *Aging Cell* **6**, 45–52  
1113 (2007).
- 1114 71. Vazquez, J. M., Kraft, M. & Lynch, V. J. A CDKN2C retroduplication in Bowhead whales is  
1115 associated with the evolution of extremely long lifespans and altered cell cycle dynamics. *bioRxiv*  
1116 2022.09.07.506958 (2022) doi:10.1101/2022.09.07.506958.
- 1117 72. Coppé, J. P., Desprez, P. Y., Król, A. & Campisi, J. The Senescence-Associated Secretory  
1118 Phenotype: The Dark Side of Tumor Suppression. *Annu Rev Pathol* **5**, 99 (2010).
- 1119 73. Mendiratta, G. *et al.* Cancer gene mutation frequencies for the U.S. population. *Nature  
1120 Communications* **2021** *12*:1, 1–11 (2021).
- 1121 74. Wright, K. M. & Deshmukh, M. Restricting Apoptosis for Postmitotic Cell Survival and its  
1122 Relevance to Cancer. <http://dx.doi.org/10.4161/cc.5.15.3129> **5**, 1616–1620 (2006).
- 1123 75. Lieber, M. R., Gu, J., Lu, H., Shimazaki, N. & Tsai, A. G. Nonhomologous DNA end joining (NHEJ)  
1124 and chromosomal translocations in humans. *Subcell Biochem* **50**, 279–296 (2014).
- 1125 76. Yoshioka, K. I., Kusumoto-Matsuo, R., Matsuno, Y. & Ishiai, M. Genomic Instability and Cancer  
1126 Risk Associated with Erroneous DNA Repair. *International Journal of Molecular Sciences* **2021**,  
1127 Vol. 22, Page 12254 **22**, 12254 (2021).
- 1128 77. Yokoyama, A. *et al.* Age-related remodelling of oesophageal epithelia by mutated cancer drivers.  
1129 *Nature* **565**, 312–317 (2019).
- 1130 78. Martincorena, I. *et al.* Somatic mutant clones colonize the human esophagus with age. *Science*  
1131 **362**, 911–917 (2018).

- 1132 79. Jaiswal, S. *et al.* Age-related clonal hematopoiesis associated with adverse outcomes. *N Engl J  
1133 Med* **371**, 2488–2498 (2014).
- 1134 80. Martincorena, I. *et al.* High burden and pervasive positive selection of somatic mutations in  
1135 normal human skin. *Science (1979)* **348**, 880–886 (2015).
- 1136 81. Mitchell, E. *et al.* Clonal dynamics of haematopoiesis across the human lifespan. *Nature* 2022  
1137 606:7913 **606**, 343–350 (2022).
- 1138 82. Kolora, S. R. R. *et al.* Origins and evolution of extreme life span in Pacific Ocean rockfishes.  
1139 *Science* **374**, 842–847 (2021).
- 1140 83. Allen, K. N. & Vázquez-Medina, J. P. Natural Tolerance to Ischemia and Hypoxemia in Diving  
1141 Mammals: A Review. *Front Physiol* **10**, 1199 (2019).
- 1142 84. Lombardi, G., Ziemann, E. & Banfi, G. Whole-Body Cryotherapy in Athletes: From Therapy to  
1143 Stimulation. An Updated Review of the Literature. *Front Physiol* **8**, 258 (2017).
- 1144 85. Gocot, R. *et al.* The Role of Deep Hypothermia in Cardiac Surgery. *Int J Environ Res Public Health*  
1145 **18**, (2021).
- 1146 86. Liu, Y. *et al.* Chronic hypoxia-induced Cirbp hypermethylation attenuates hypothermic  
1147 cardioprotection via down-regulation of ubiquinone biosynthesis. *Sci Transl Med* **11**, (2019).
- 1148 87. Wu, L. *et al.* Therapeutic Hypothermia Enhances Cold-Inducible RNA-Binding Protein Expression  
1149 and Inhibits Mitochondrial Apoptosis in a Rat Model of Cardiac Arrest. *Mol Neurobiol* **54**, 2697–  
1150 2705 (2017).
- 1151 88. Yu, L., Gu, T., Liu, Y., Jiang, X. & Shi, E. Cold-inducible ribonucleic acid-binding protein attenuates  
1152 acute kidney injuries after deep hypothermic circulatory arrest in rats. *Interact Cardiovasc Thorac  
1153 Surg* **26**, 124–130 (2018).
- 1154 89. Li, Y. *et al.* Cold-inducible RNA-binding protein maintains intestinal barrier during deep  
1155 hypothermic circulatory arrest. *Interact Cardiovasc Thorac Surg* **29**, 583–591 (2019).
- 1156 90. Pan, H. Z. *et al.* Cold-inducible RNA binding protein agonist enhances the cardioprotective effect  
1157 of UW solution during extended heart preservation. *Artif Organs* **44**, E406–E418 (2020).
- 1158 91. Chen, Y. *et al.* Fight to the bitter end: DNA repair and aging. *Ageing Res Rev* **64**, 101154 (2020).
- 1159 92. Seluanov, A., Vaidya, A. & Gorbunova, V. Establishing Primary Adult Fibroblast Cultures From  
1160 Rodents. *J Vis Exp* **44**, (2010).
- 1161 93. Quail, M. A. *et al.* Optimal enzymes for amplifying sequencing libraries. *Nat Methods* **9**, 10–11  
1162 (2012).
- 1163 94. Blackburn, M. C. Development of new tools and applications for high-throughput sequencing of  
1164 microbiomes in environmental or clinical samples. (2010).
- 1165 95. Clement, K. *et al.* CRISPResso2 provides accurate and rapid genome editing sequence analysis.  
1166 *Nature Biotechnology* 2019 37:3 **37**, 224–226 (2019).

- 1167 96. Lee, H. J., Chang, H. Y., Cho, S. W. & Ji, H. P. CRISPRpic: fast and precise analysis for CRISPR-  
1168 induced mutations via prefixed index counting. *NAR Genom Bioinform* **2**, (2020).
- 1169 97. GitHub - jstjohn/SeqPrep: Tool for stripping adaptors and/or merging paired reads with overlap  
1170 into single reads. <https://github.com/jstjohn/SeqPrep>.
- 1171 98. Franken, N. A. P., Rodermond, H. M., Stap, J., Haveman, J. & van Bree, C. Clonogenic assay of cells  
1172 in vitro. *Nat Protoc* **1**, 2315–2319 (2006).
- 1173 99. Rose, J. C. *et al.* Rapidly inducible Cas9 and DSB-ddPCR to probe editing kinetics. *Nat Methods* **14**,  
1174 891 (2017).
- 1175 100. Hudon, S. F. *et al.* Primers to highly conserved elements optimized for qPCR-based telomere  
1176 length measurement in vertebrates. *Mol Ecol Resour* **21**, 59–67 (2021).
- 1177 101. Dimri, G. P. *et al.* A biomarker that identifies senescent human cells in culture and in aging skin in  
1178 vivo. *Proc Natl Acad Sci U S A* **92**, 9363 (1995).
- 1179 102. Debacq-Chainiaux, F., Erusalimsky, J. D., Campisi, J. & Toussaint, O. Protocols to detect  
1180 senescence-associated beta-galactosidase (SA- $\beta$ gal) activity, a biomarker of senescent cells in  
1181 culture and in vivo. *Nature Protocols* **2009 4:12 4**, 1798–1806 (2009).
- 1182 103. Mao, Z. *et al.* SIRT6 promotes DNA repair under stress by activating PARP1. *Science (1979)* **332**,  
1183 1443–1446 (2011).
- 1184 104. Benchling. <https://www.benchling.com/>.
- 1185 105. Patro, R., Duggal, G., Love, M. I., Irizarry, R. A. & Kingsford, C. Salmon provides fast and bias-  
1186 aware quantification of transcript expression. *Nature Methods* **2017 14:4 14**, 417–419 (2017).
- 1187 106. Lu, J. Y. *et al.* Comparative transcriptomics reveals circadian and pluripotency networks as two  
1188 pillars of longevity regulation. *Cell Metab* **34**, 836-856.e5 (2022).
- 1189 107. Robinson, M. D., McCarthy, D. J. & Smyth, G. K. edgeR: a Bioconductor package for differential  
1190 expression analysis of digital gene expression data. *Bioinformatics* **26**, 139–140 (2010).
- 1191 108. Love, M. I., Huber, W. & Anders, S. Moderated estimation of fold change and dispersion for RNA-  
1192 seq data with DESeq2. *Genome Biol* **15**, 1–21 (2014).
- 1193 109. Escher, C. *et al.* Using iRT, a normalized retention time for more targeted measurement of  
1194 peptides. *Proteomics* **12**, 1111–1121 (2012).
- 1195 110. Kong, A. T., Leprevost, F. v., Avtonomov, D. M., Mellacheruvu, D. & Nesvizhskii, A. I. MSFragger:  
1196 ultrafast and comprehensive peptide identification in mass spectrometry-based proteomics.  
1197 *Nature Methods* **2017 14:5 14**, 513–520 (2017).
- 1198 111. Teo, G. C., Polasky, D. A., Yu, F. & Nesvizhskii, A. I. Fast Deisotoping Algorithm and Its  
1199 Implementation in the MSFragger Search Engine. *J Proteome Res* **20**, 498–505 (2021).

- 1200 112. Yu, F., Haynes, S. E. & Nesvizhskii, A. I. IonQuant enables accurate and sensitive label-free  
1201 quantification with FDR-controlled match-between-runs. *Molecular and Cellular Proteomics* **20**,  
1202 100077 (2021).
- 1203 113. da Veiga Leprevost, F. et al. Philosopher: a versatile toolkit for shotgun proteomics data analysis.  
1204 *Nature Methods* 2020 **17**:9 **17**, 869–870 (2020).
- 1205 114. The Bowhead Whale Genome Resource. <http://www.bowhead-whale.org/>.
- 1206 115. Haas, B. J. et al. De novo transcript sequence reconstruction from RNA-seq using the Trinity  
1207 platform for reference generation and analysis. *Nature Protocols* 2013 **8**:8 **8**, 1494–1512 (2013).
- 1208 116. Grabherr, M. G. et al. Full-length transcriptome assembly from RNA-Seq data without a reference  
1209 genome. *Nature Biotechnology* 2011 **29**:7 **29**, 644–652 (2011).
- 1210 117. Bateman, A. et al. UniProt: the universal protein knowledgebase in 2021. *Nucleic Acids Res* **49**,  
1211 D480–D489 (2021).
- 1212 118. Elias, J. E. & Gygi, S. P. Target-decoy search strategy for increased confidence in large-scale  
1213 protein identifications by mass spectrometry. *Nature Methods* 2007 **4**:3 **4**, 207–214 (2007).
- 1214

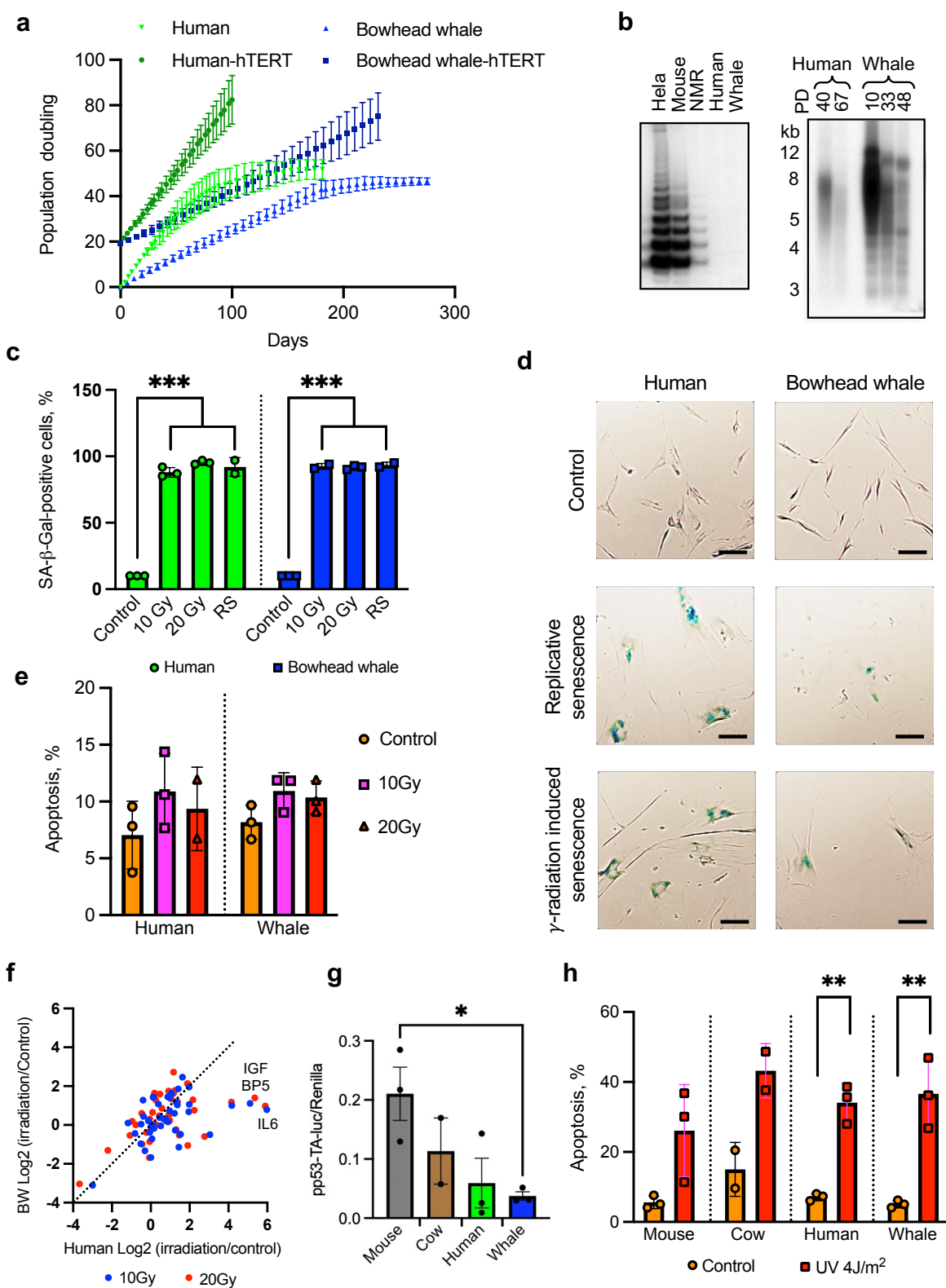


**Figure 1. Bowhead whale fibroblasts exhibit senescence with reduced SASP and low p53 activity. a, Growth curves of primary and hTERT-immortalized skin fibroblasts**

(n=2 for each cell line). **b**, Telomerase activity and telomere length in skin fibroblasts. **c**, Quantification of  $\beta$ -gal-positive human and bowhead skin fibroblasts in response to  $\gamma$ -irradiation (12 days) and replicative senescence (n=3 for each species). **d**, Representative images of SA- $\beta$ -gal staining of human and bowhead skin fibroblasts in response to  $\gamma$ -irradiation and replicative senescence. The bar is 100  $\mu$ m. **e**, Apoptosis of human and bowhead whale fibroblasts in response to  $\gamma$ -irradiation. Three days after  $\gamma$ -irradiation, cells were harvested and subjected to an Annexin V apoptosis assay using flow cytometry (n=3 for each species). **f**, Log fold change of SASP mRNA expression in human and bowhead whale skin fibroblasts 12 days after  $\gamma$ -irradiation. **g**, Relative luciferase expression in mouse, cow, human and bowhead whale fibroblasts transfected with the p53 reporter vector. Data are shown as ratios of firefly/renilla luciferase (to normalize for transfection efficiency) expression 24 h after transfections (n=3 for mouse, human, BW; n=2 for cow). **h**, Apoptosis of mouse, cow, human and bowhead whale fibroblasts in response to UVC. Two days after UVC, cells were harvested and subjected to an Annexin V apoptosis assay using flow cytometry. Error bars represent mean  $\pm$  SD. \* p<0.05, \*\* p<0.01, \*\*\* p<0.001. Two-tailed t-test was used to quantify the significance. Whale, bowhead whale; NMR, naked mole-rat.

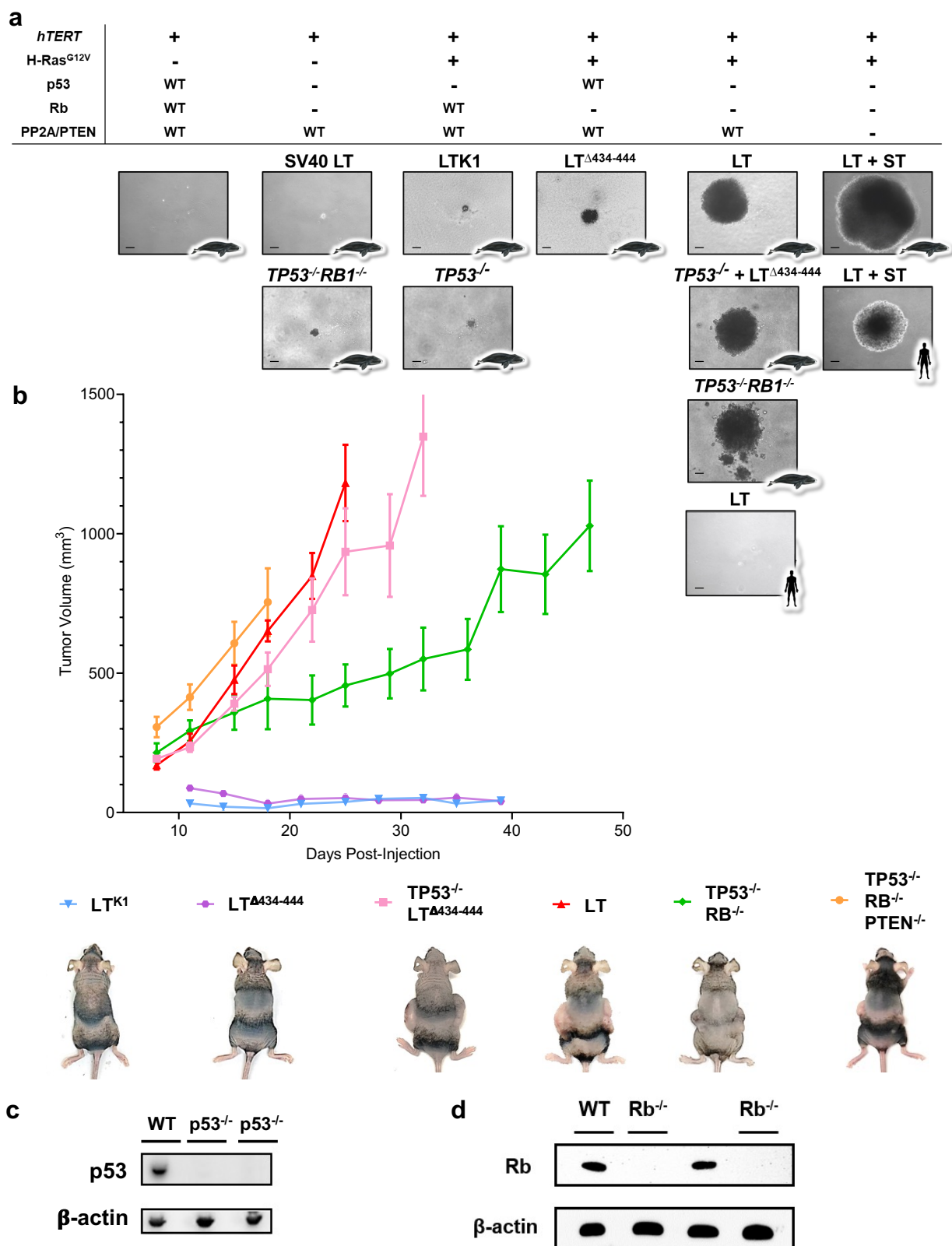


**Figure 2. Fewer hits are required for oncogenic transformation of bowhead whale fibroblasts than for human fibroblasts.** **a**, Images of representative fibroblast colonies for tested cell lines after 4 weeks of growth in soft agar. The top panel indicates whether the cell lines in the column below have the indicated protein overexpressed (+), inactivated (-), or expressed in the active endogenous form (WT). Text above individual images indicate for that cell line whether tumor suppressors are inactivated through genetic knockout or SV40 Large T (or LT mutants) or Small T (ST) antigen. Icons in corners of images indicate species. Scale bar is 250  $\mu$ m. **b**, Volumetric growth curves for the indicated bowhead whale fibroblast cell lines in mouse xenograft assays. All cell lines shown stably express H-Ras<sup>G12V</sup> and *hTERT* in addition to the genotype indicated in the figure legend. Data points represent averages from 3 immunodeficient nude mice injected bilaterally (6 injections) for each cell line, except for *TP53*<sup>-/-</sup>/*RB1*<sup>-/-</sup> double knockouts, for which 2 independent cell lines were tested, for a total of 6 mice/12 injections. Experiments were terminated based on endpoints for maximum tumor size or duration of experiment as described in Methods. Images in the legend show a representative mouse for the indicated cell line at the final measured time point. Error bars show SEM. **c**, Western blot for p53 protein in clonally isolated fibroblast colonies following CRISPR targeting of *TP53*. Underlined lanes indicate colonies selected for further validation and experiments. **d**, Western blot for Rb protein in fibroblast clones following CRISPR targeting of *RB1* on an p53 knockout background.

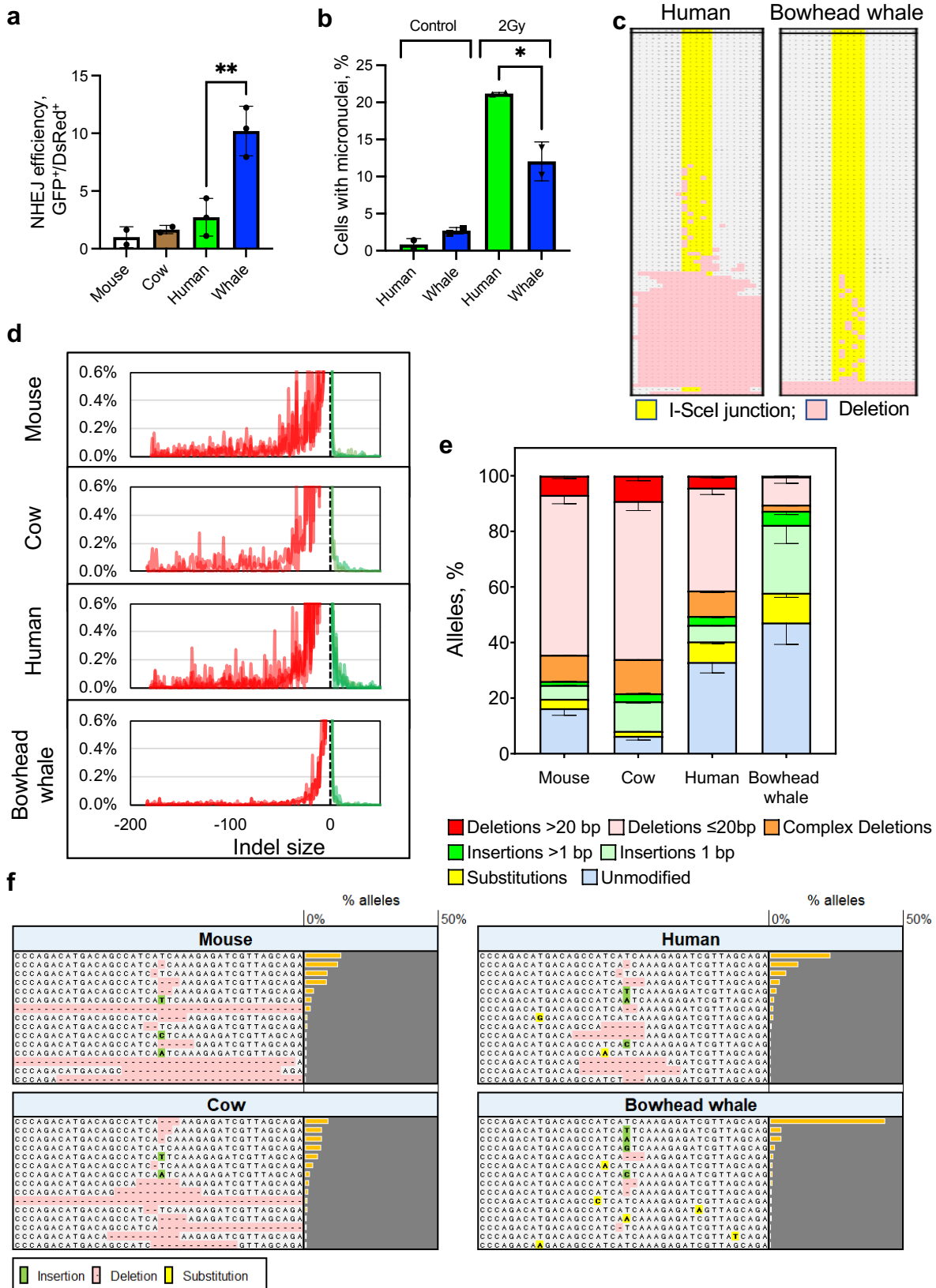


**Figure 3. The bowhead whale repairs DSBs with higher accuracy and efficiency than other mammals.** **a**, NHEJ efficiency was measured using fluorescent reporter construct where GFP gene is interrupted by a “killer” exon flanked by I-SceI sites (Extended Data Figure 3a). DSB induction by I-SceI removes the exon and successful NHEJ event leads to reactivation of the GFP gene. NHEJ reporter construct was integrated into primary, low passage skin fibroblasts. NHEJ repair efficiency was assayed by transfecting cells with I-SceI expression vector and a DsRed plasmid as a transfection control. The repair efficiency was calculated as the ratio of GFP+/DsRed+ cells. Experiments were repeated at least 3 times for each cell line. **b**, % binucleated cells containing micronuclei in human and bowhead whale fibroblasts after 2Gy  $\gamma$ -irradiation. Error bars represent SD ( $n=2$ ). **c**, Allele plot of Sanger sequencing products resulting from repair of integrated NHEJ reporter cassette after I-SceI cleavage. **d**, Histograms of CRISPR indel size distribution by species. Data for biological replicates are superimposed and partially transparent with lines connecting data points for each sample. Unmodified alleles and alleles with substitutions only are excluded from this analysis. **e**, Distribution of sequenced PTEN allele variants by species after CRISPR DSB induction at a conserved region of the endogenous PTEN gene. Data are averages from multiple primary dermal fibroblast lines isolated from different individual animals for bowhead whale ( $n=3$ ), human ( $n=3$ ), cow ( $n=2$ ), and mouse ( $n=3$ ). Error bars represent SEM. **f**, Allele plots showing 15 most frequent allele types after CRISPR for one representative cell line per species. Sequences are displayed within a window centered on the cleavage site and extending 20 bp in each direction. Data bars and values indicate proportion of total alleles represented by each row. For the purposes of this display and quantification, all individual alleles with identical sequences in the 40-bp window have been pooled, so rows represent composites of alleles that may differ outside the display window. Error bars represent SD. \*  $p<0.05$ , \*\*  $p<0.01$  (two-tailed t-test). Whale, bowhead whale.

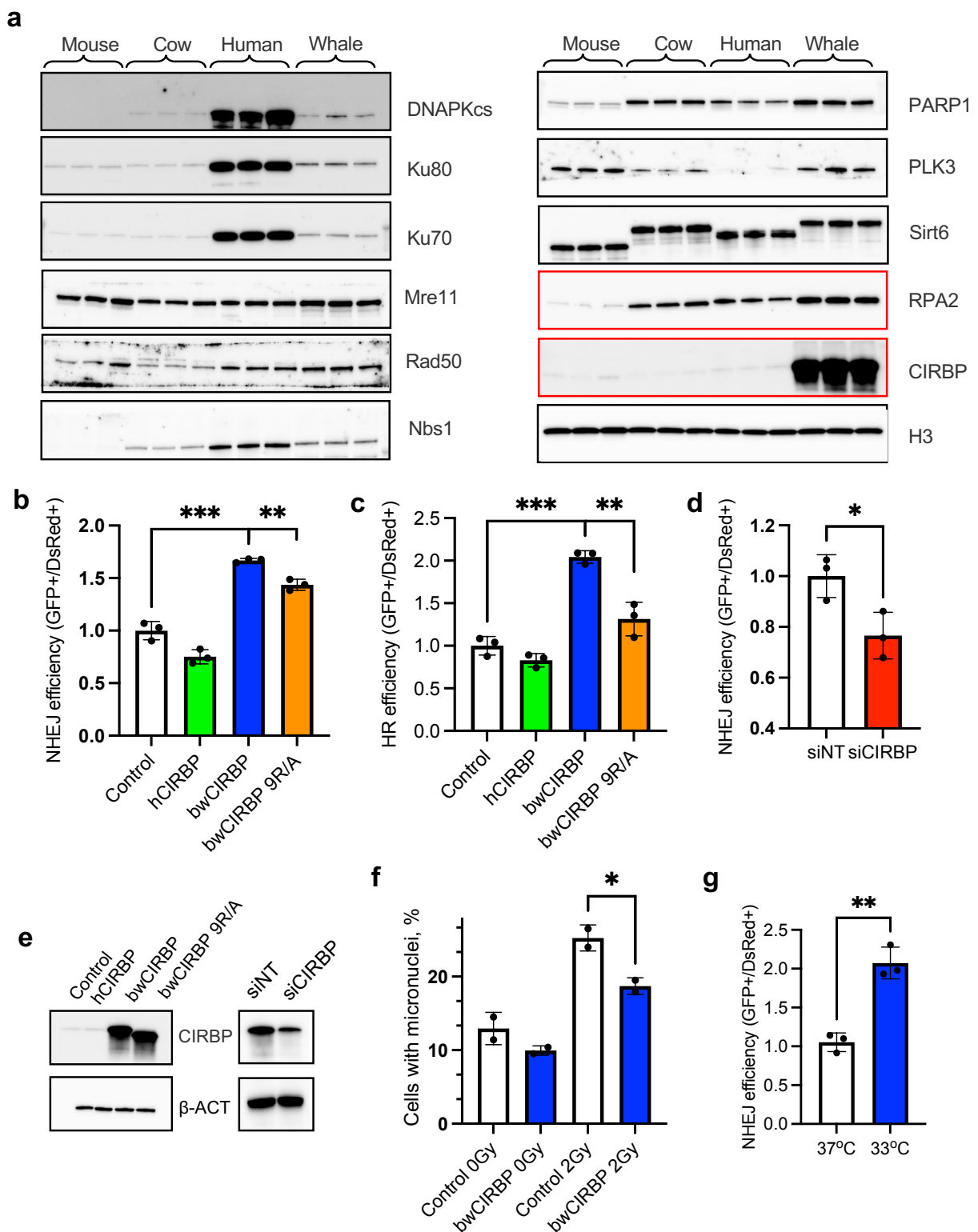


**Figure 4. CIRBP is highly expressed in bowhead whale fibroblasts and promotes genomic stability.** **a**, Western blots of DNA repair proteins in primary fibroblasts from different species. **b-c**, bwCIRBP promotes NHEJ and HR in human cells as measured by

flow cytometric GFP-reporter assays (see Methods). In these assays DSBs are induced within inactive NHEJ or HR reporter cassettes by expressing I-SceI endonuclease. Successful NHEJ or HR events lead to reactivation of the fluorescent GFP reporters that are scored by flow cytometry. All experiments in these figures were repeated at least 3 times. **d**, Knockdown of CIRBP in bowhead whale fibroblasts decreases NHEJ efficiency. Cells were transfected with siRNA 3d before I-Sce1 transfection. **e**, Western blot of human fibroblasts overexpressing human CIRBP, whale CIRBP or 9R/A mutated whale CIRBP (left panel); and bowhead whale fibroblasts with knockdown of CIRBP (right panel). **f**, Overexpression of bwCIRBP decreases the percentage of human cells containing micronuclei 3d after 2Gy  $\gamma$ -irradiation (n=2). **g**, Hypothermia promotes NHEJ efficiency in primary human fibroblasts. Cells were pre-incubated at 33°C for 2 days, co-transfected with I-SceI-digested NHEJ reporter and DsRed, and returned to the 33°C incubator. NHEJ efficiency was measured by flow cytometry 3 days following transfection (n=3). Error bars represent mean  $\pm$  SD. \* p<0.05, \*\* p<0.01, \*\*\* p<0.001 (two-tailed t-test).

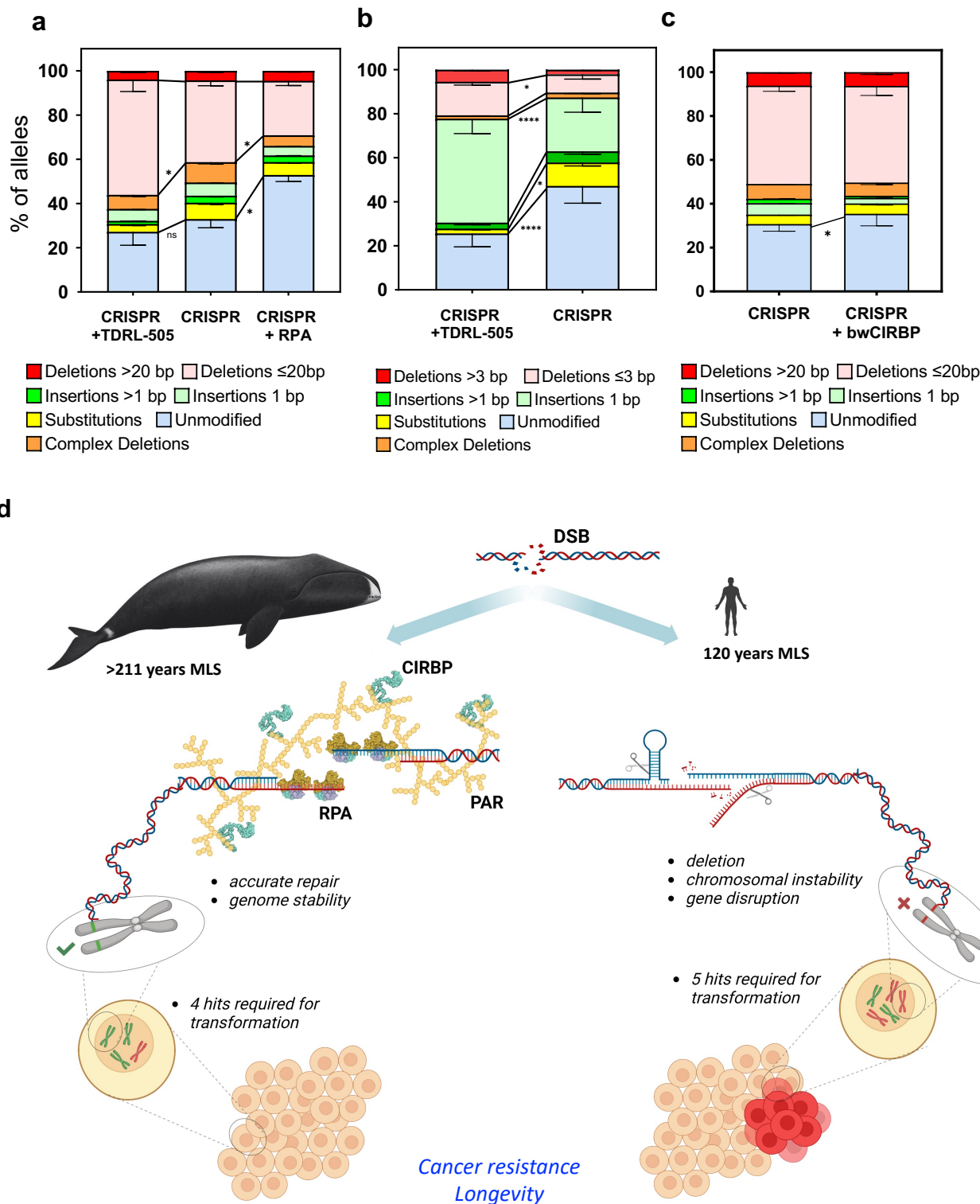
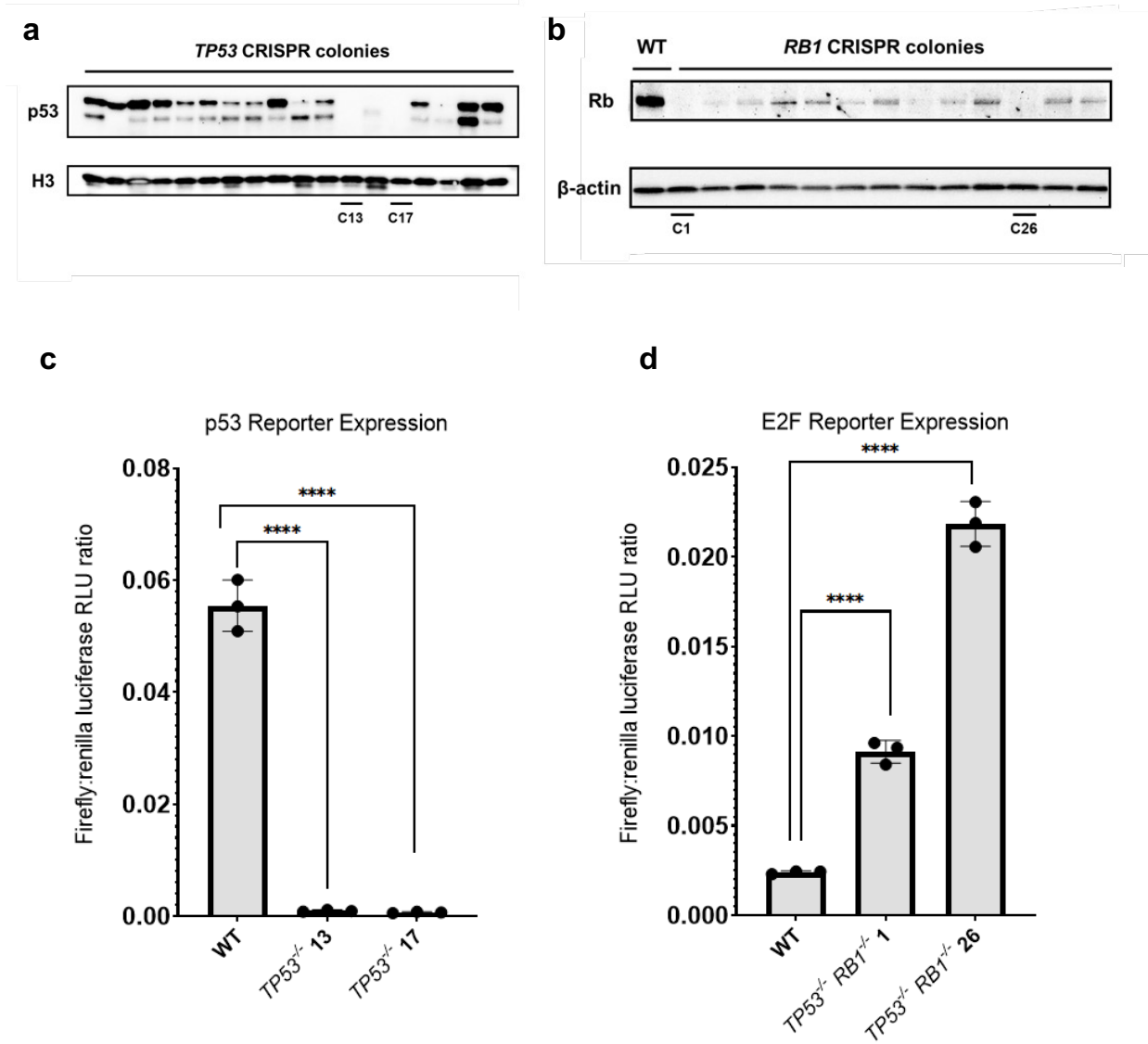


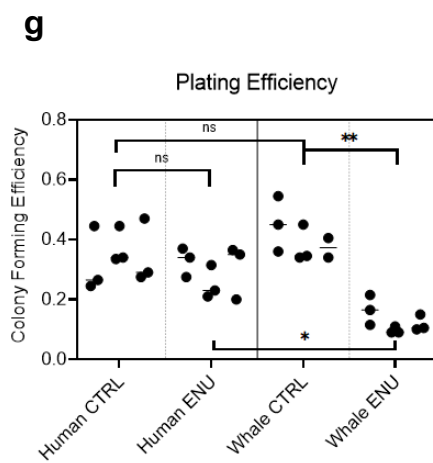
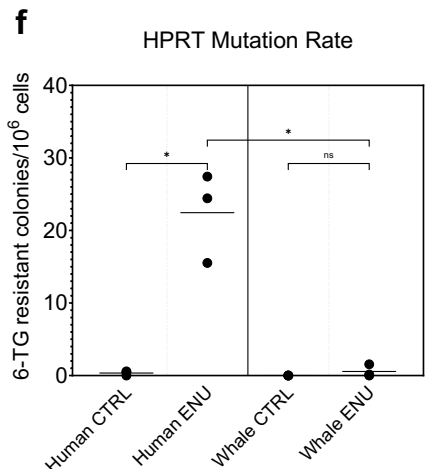
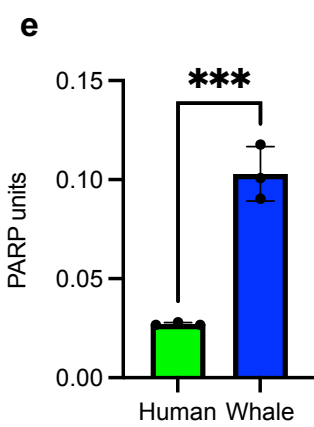
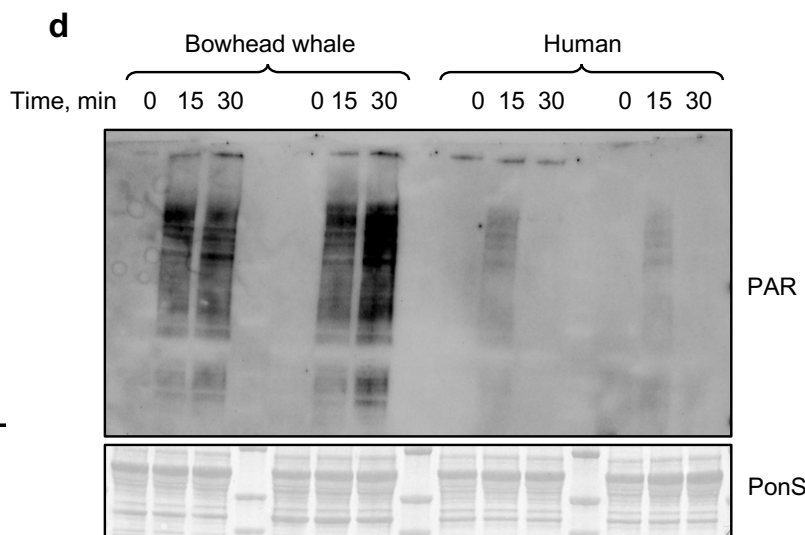
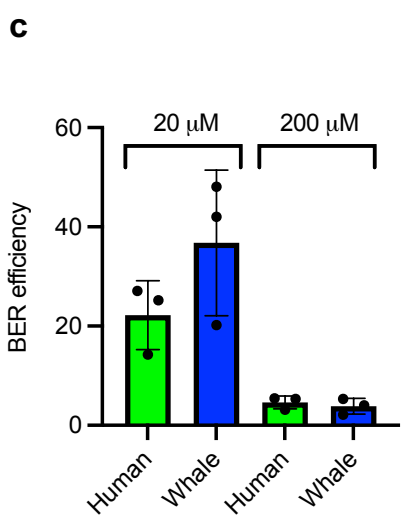
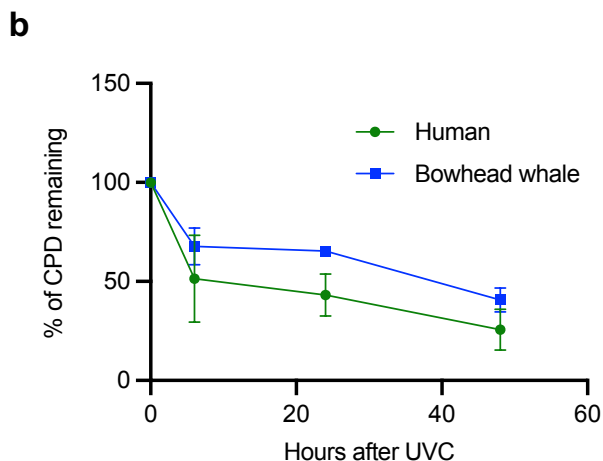
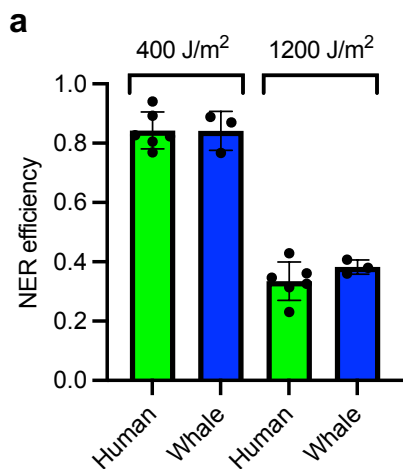
**Figure 5. RPA and CIRBP contribute to increased DNA repair fidelity.** **a**, Distribution of sequenced PTEN allele variants in human primary fibroblasts treated with RPA inhibitor TDRL-505 or transfected with human RPA complex after CRISPR DSB induction at a

conserved region of the endogenous PTEN gene. **b**, Distribution of sequenced PTEN allele variants by species in bowhead whale primary fibroblasts treated with TDRL-505 after CRISPR DSB induction in PTEN gene. **c**, Distribution of sequenced PTEN allele variants by species in human fibroblasts with lentiviral overexpression of luciferase or bwCIRBP after CRISPR DSB induction in endogenous PTEN gene. **(a-c)** Data are averages from experiments performed in triplicate. Error bars represent SEM. \* p<0.05, \*\*\*\* p<0.0001. All charts analyzed by two-way ANOVA with Fisher's LSD.

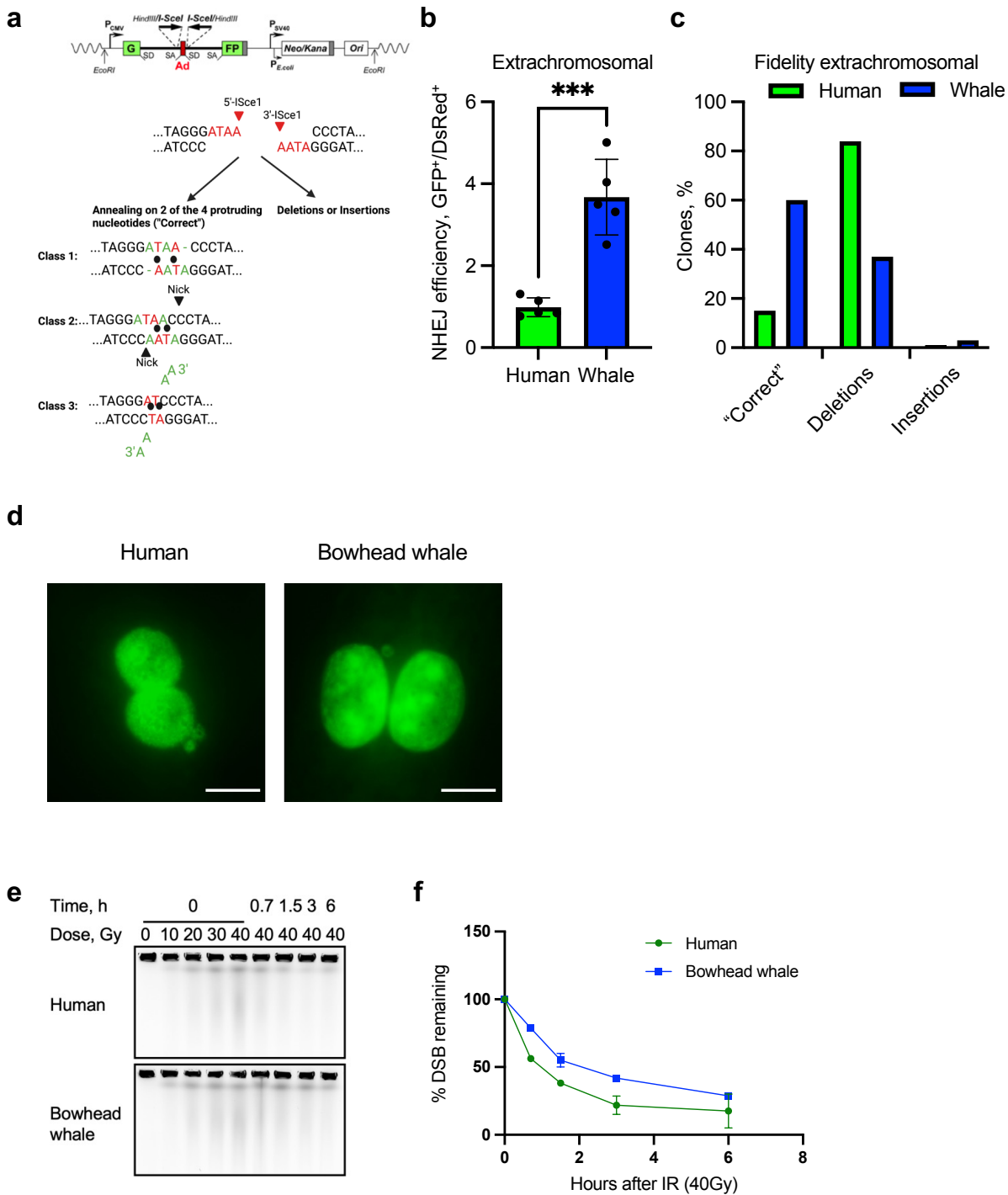
**d**, Graphical summary. Bowhead whale has evolved very efficient and accurate DSB repair that is mediated by high protein levels of CIRBP, RPA2 and high PARP activity. This enhanced DNA repair may help bowhead whale achieve cancer resistance despite fewer mutational hits required for malignant transformation of whale cells as compared to human cells. The strategy of enhanced repair rather than enhanced elimination of damaged cells through apoptosis or senescence may benefit the extreme longevity of the bowhead whale.



**Extended Data Figure 1. Characterization of p53 and Rb knockout cell lines.** **a**, Western blot for p53 protein in fibroblasts clones following CRISPR targeting of *TP53*. Labeled clones were for further validation and experiments. **b**, Western blot for Rb protein in fibroblast clones following CRISPR targeting of *RB1* on p53 knockout background. **c**, Ratio of firefly:renilla luciferase luminescence in fibroblasts transfected with firefly luciferase reporter of p53 transcriptional activity and renilla luciferase control. Cells were treated with etoposide to induce p53 activity. **d**, Ratio of firefly:renilla luciferase luminescence in fibroblasts transfected with firefly luciferase reporter of E2F transcriptional activity and renilla luciferase control. Transfected cells were serum starved for 24h and returned to complete medium for 24h before luminescence measurement. Higher E2F activity results from reduced Rb activity. Error bars represent SD. \*\*\*\*p<0.001 (two-tailed t test), n=3.



**Extended Data Figure 2. Analysis of NER and BER in bowhead whale cells.** **a**, NER efficiency was measured by host cell reactivation assay where a plasmid containing luciferase reporter is UV-irradiated *in vitro* to induce DNA damage, transfected into cells, and reactivation of the reporter is measured ( $n=3$  for each cell line). **b**, Kinetics of cyclobutane pyrimidine dimer repair after 30 J/m<sup>2</sup> UVC. Confluent human and whale skin fibroblasts were subjected to UVC, harvested at different time-points, genomic DNA was isolated and analyzed for cyclobutene dimers as described in Methods ( $n=2$  for each cell line). **c**, BER efficiency was measured by host cell reactivation where luciferase reporter plasmid is treated with methylene blue and light to induce oxidative DNA damage, transfected into cells, and luciferase activity measured as described in Methods. **d**, Bowhead whale cells show greater poly-ADP-ribosylation in response to hydrogen peroxide treatment. **e**, Nuclear extracts of bowhead whale fibroblasts exhibit higher basal PARP activity ( $n=3$ ). **f**, HPRT mutagenesis assay, adjusted by plating efficiency measured for each cell line. **g**, Colony forming efficiency for HPRT mutagenesis assay. Error bars represent mean  $\pm$  SD. \*  $p<0.05$ , \*\*  $p<0.01$ , \*\*\*  $p<0.001$ , ns=not significant (two-tailed t-test).

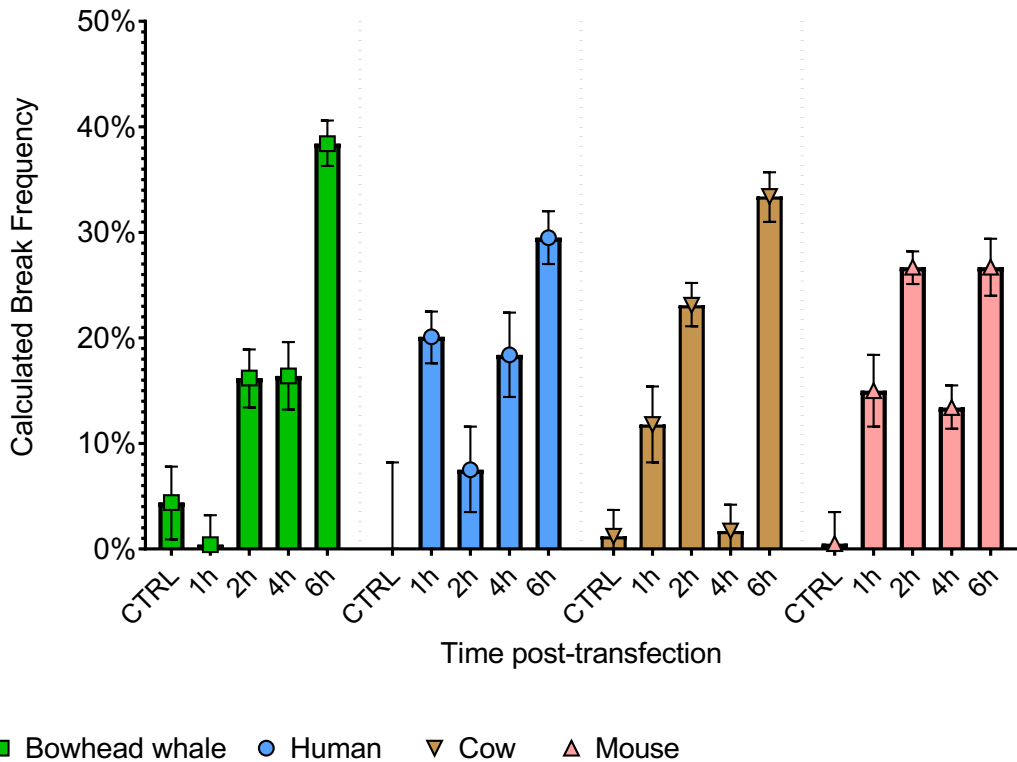


**Extended Data Figure 3. Analysis of DSB repair in bowhead whale cells.** **a**, Possible repair outcomes after induction of DSBs with incompatible ends by I-SceI in NHEJ reporter construct. **b**, NHEJ efficiency in extrachromosomal assay. NHEJ reporter construct was pre-digested with I-SceI, purified and co-transfected with DsRed into human and bowhead skin fibroblasts. Three days after transfection cells were harvested and subjected to flow cytometry to calculate NHEJ efficiency ( $n=3$ ). **c**, NHEJ fidelity in

extrachromosomal assay. Immediately after FACS/flow cytometry, genomic DNA was isolated, subjected to PCR, cloned and analyzed by Sanger sequencing. At least 100 clones were analyzed for each species. **d**, Representative images of human and bowhead whale binucleated cells containing micronuclei after 2 Gy of  $\gamma$ -irradiation. Scale bar is 20  $\mu\text{m}$ . **e**, Pulse-field gel stained with ethidium bromide, showing chromosomal DNA fragmentation in human and bowhead confluent skin fibroblasts immediately after different doses of  $\gamma$ -irradiation 0.7, 1.5, 3 and 6h after 40 Gy of  $\gamma$ -irradiation. **f**, Kinetics of DSB repair measured by PFGE in confluent human and bowhead fibroblasts after 40 Gy of  $\gamma$ -irradiation. n=2 for each species. Error bars represent mean  $\pm$  SD. \*\*\* p<0.001 (two-tailed t-test).



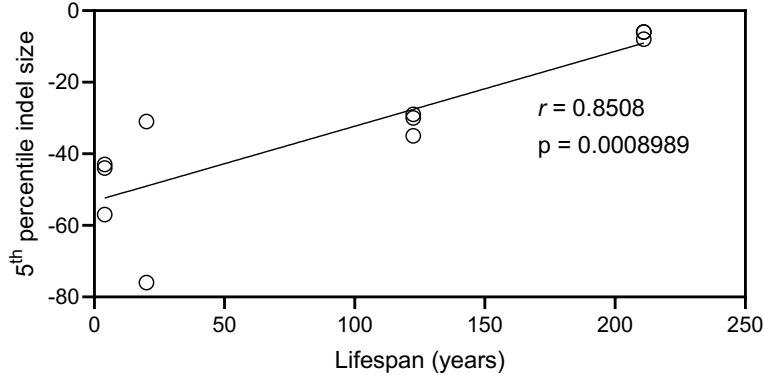
**Extended Data Figure 4. *PTEN* sequences used for CRISPR NHEJ assays.** **a**, Alignment of NGS amplicon sequences for each species used to measure NHEJ repair fidelity, showing *PTEN* Exon 1 and guide RNA target site. Amplicon/primer pair was designed based on size appropriate for paired-end sequencing, conservation of internal sequence and primer binding sites, and optimal positioning to detect large deletions. Mismatches to consensus sequence are highlighted in red. Alignments are shown in Benchling with Clustal Omega. **b**, Allele plots from untreated (wild-type) control samples for each species. Plots are outputs from CRISPResso2.



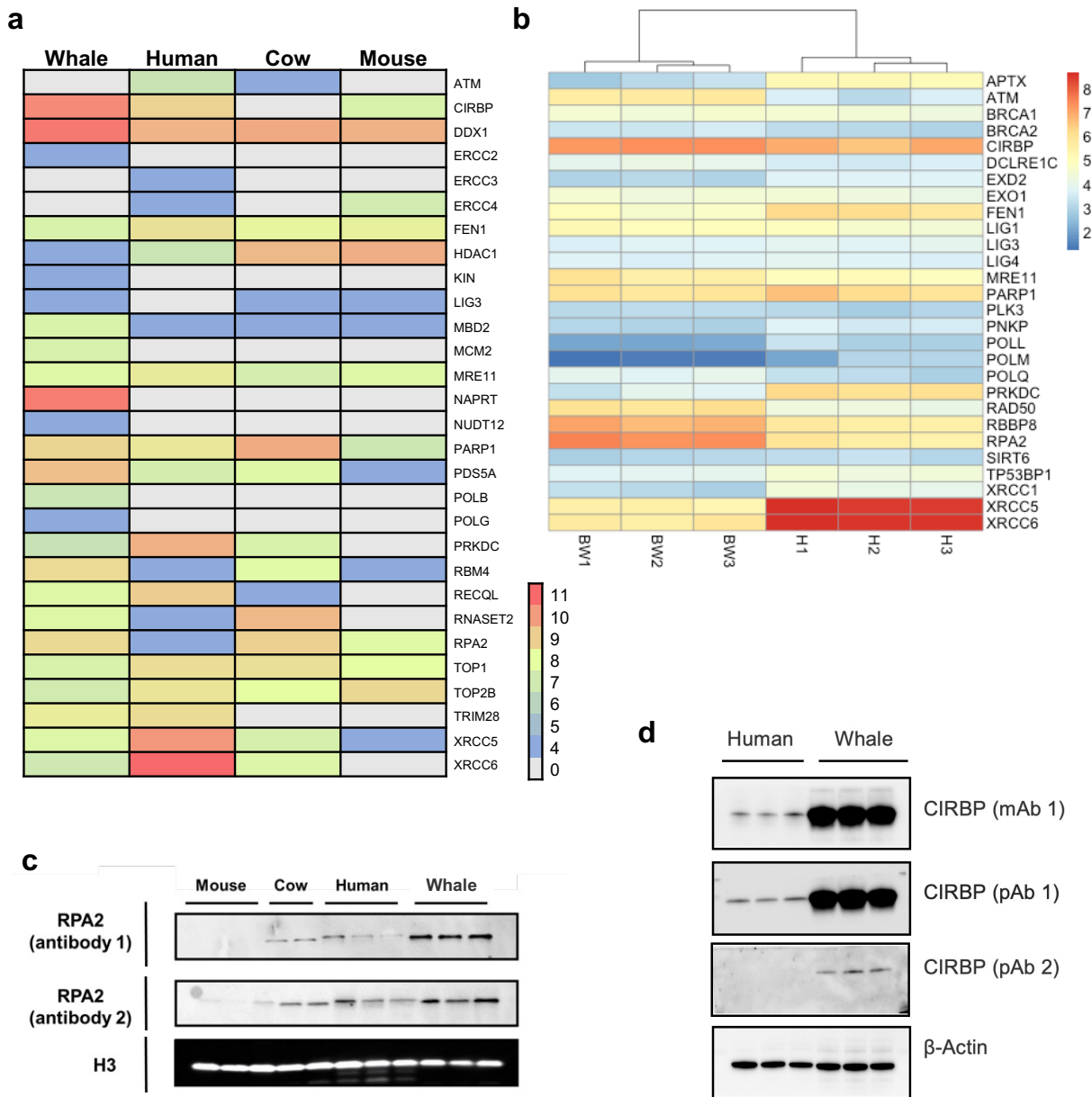
**Extended Data Figure 5. Analysis of CRISPR cutting efficiency in different species.**  
 Time course of CRISPR cleavage measured by digital droplet PCR (ddPCR). PTEN copy number at varying time points after CRISPR RNP transfection was measured with ddPCR using primers flanking the predicted cleavage site and normalized within each sample to a single-copy genomic ultra-conserved element as described in Methods. Error bars show confidence intervals of Poisson distribution calculated in QuantaSoft. Data are averages from experiments performed in triplicate.

**a**

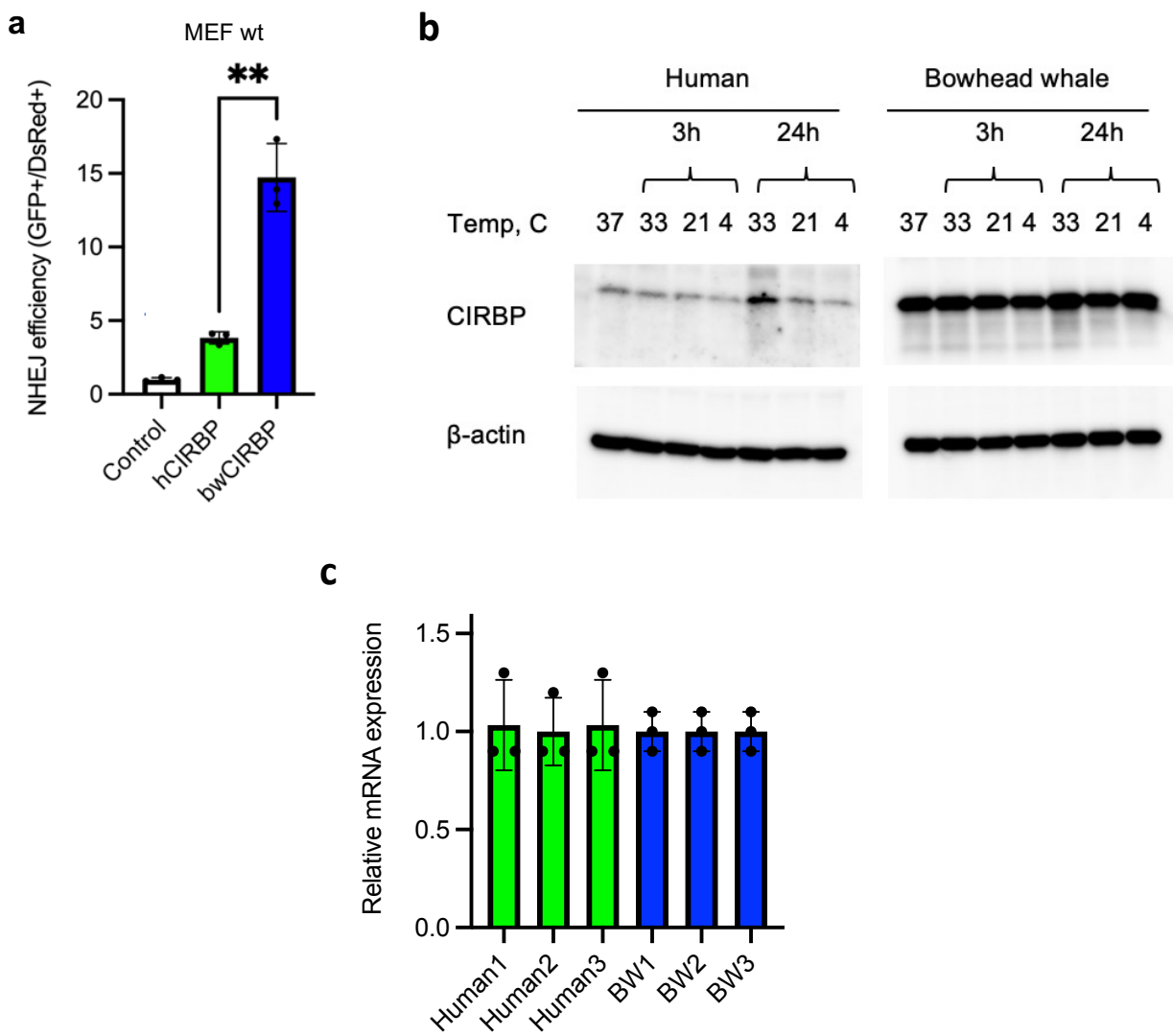
	Mouse				Cow			Human				Bowhead whale			
	WTMSF9	WTMSF10	BL6MSF2	Avg.	BT1SF	BT2SF	Avg.	NHDF	HDF637	YAHSF	Avg.	18B9SF	14B10SF	14B11SF	Avg.
<b>1%</b>	-142.0	-140.0	-134.0	<b>-138.7</b>	-154.0	-121.0	<b>-137.5</b>	-104.0	-126.0	-133.0	<b>-121.0</b>	-38.0	-30.0	-68.0	<b>-45.3</b>
<b>2%</b>	-110.0	-113.0	-105.0	<b>-109.3</b>	-134.0	-82.0	<b>-108.0</b>	-63.0	-88.0	-102.0	<b>-84.3</b>	-15.0	-14.0	-24.0	<b>-17.7</b>
<b>3%</b>	-84.0	-92.0	-80.0	<b>-85.3</b>	-112.0	-43.0	<b>-77.5</b>	-41.0	-60.0	-71.0	<b>-57.3</b>	-10.0	-10.0	-16.0	<b>-12.0</b>
<b>4%</b>	-60.0	-80.0	-55.0	<b>-65.0</b>	-93.0	-34.0	<b>-63.5</b>	-34.0	-37.0	-46.0	<b>-39.0</b>	-7.0	-8.0	-11.0	<b>-8.7</b>
<b>5%</b>	-44.0	-57.0	-43.0	<b>-48.0</b>	-76.0	-31.0	<b>-53.5</b>	-29.0	-30.0	-35.0	<b>-31.3</b>	-6.0	-6.0	-8.0	<b>-6.7</b>
<b>6%</b>	-34.0	-44.0	-34.0	<b>-37.3</b>	-54.0	-26.0	<b>-40.0</b>	-25.0	-25.0	-30.0	<b>-26.7</b>	-4.0	-5.0	-7.0	<b>-5.3</b>
<b>7%</b>	-26.0	-38.0	-29.0	<b>-31.0</b>	-42.0	-25.0	<b>-33.5</b>	-22.0	-23.0	-25.0	<b>-23.3</b>	-3.0	-4.0	-6.0	<b>-4.3</b>
<b>8%</b>	-21.0	-34.0	-22.0	<b>-25.7</b>	-36.0	-22.0	<b>-29.0</b>	-21.0	-21.0	-23.0	<b>-21.7</b>	-3.0	-3.0	-4.0	<b>-3.3</b>
<b>9%</b>	-16.0	-29.0	-18.0	<b>-21.0</b>	-31.0	-21.0	<b>-26.0</b>	-18.0	-18.0	-22.0	<b>-19.3</b>	-3.0	-3.0	-3.0	<b>-3.0</b>
<b>10%</b>	-12.0	-25.0	-14.0	<b>-17.0</b>	-26.0	-19.0	<b>-22.5</b>	-16.0	-16.0	-21.0	<b>-17.7</b>	-3.0	-3.0	-3.0	<b>-3.0</b>
<b>15%</b>	-4.0	-14.0	-5.0	<b>-7.7</b>	-18.0	-12.0	<b>-15.0</b>	-10.0	-10.0	-13.0	<b>-11.0</b>	-2.0	-3.0	-3.0	<b>-2.7</b>
<b>20%</b>	-3.0	-6.0	-3.0	<b>-4.0</b>	-12.0	-9.0	<b>-10.5</b>	-6.0	-6.0	-10.0	<b>-7.3</b>	-1.0	-2.0	-2.0	<b>-1.7</b>
<b>25%</b>	-3.0	-4.0	-3.0	<b>-3.3</b>	-10.0	-5.0	<b>-7.5</b>	-3.0	-3.0	-6.0	<b>-4.0</b>	1.0	-1.0	-1.0	<b>-0.3</b>
<b>30%</b>	-3.0	-3.0	-3.0	<b>-3.0</b>	-7.0	-3.0	<b>-5.0</b>	-3.0	-3.0	-4.0	<b>-3.3</b>	1.0	-1.0	1.0	<b>0.3</b>
<b>35%</b>	-2.0	-3.0	-3.0	<b>-2.7</b>	-5.0	-3.0	<b>-4.0</b>	-2.0	-2.0	-3.0	<b>-2.3</b>	1.0	-1.0	1.0	<b>0.3</b>
<b>40%</b>	-2.0	-3.0	-2.0	<b>-2.3</b>	-3.0	-3.0	<b>-3.0</b>	-1.0	-1.0	-3.0	<b>-1.7</b>	1.0	-1.0	1.0	<b>0.3</b>
<b>50%</b>	-1.0	-2.0	-1.0	<b>-1.3</b>	-3.0	-2.0	<b>-2.5</b>	-1.0	-1.0	-3.0	<b>-1.7</b>	1.0	1.0	1.0	<b>1.0</b>
<b>60%</b>	-1.0	-1.0	-1.0	<b>-1.0</b>	-2.0	-1.0	<b>-1.5</b>	-1.0	-1.0	-1.0	<b>-1.0</b>	1.0	1.0	1.0	<b>1.0</b>
<b>70%</b>	-1.0	-1.0	-1.0	<b>-1.0</b>	-1.0	-1.0	<b>-1.0</b>	-1.0	-1.0	-1.0	<b>-1.0</b>	1.0	1.0	1.0	<b>1.0</b>
<b>85%</b>	-1.0	-1.0	-1.0	<b>-1.0</b>	-1.0	1.0	<b>0.0</b>	1.0	-1.0	1.0	<b>0.3</b>	1.0	1.0	1.0	<b>1.0</b>
<b>90%</b>	-1.0	-1.0	-1.0	<b>-1.0</b>	1.0	1.0	<b>1.0</b>	1.0	1.0	1.0	<b>1.0</b>	1.0	1.0	1.0	<b>1.0</b>
<b>95%</b>	1.0	1.0	1.0	<b>1.0</b>	1.0	1.0	<b>1.0</b>	1.0	1.0	1.0	<b>1.0</b>	1.0	1.0	1.0	<b>1.0</b>

**b**

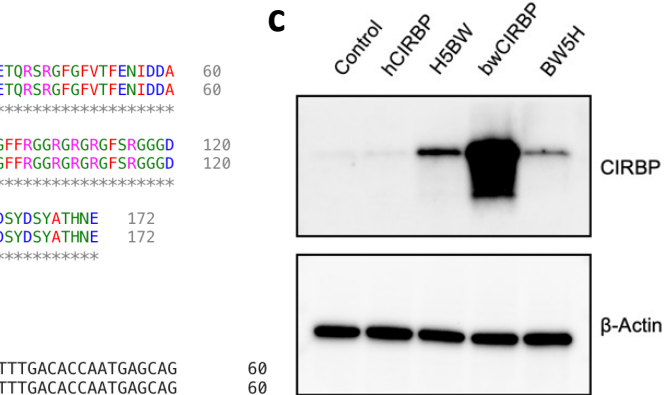
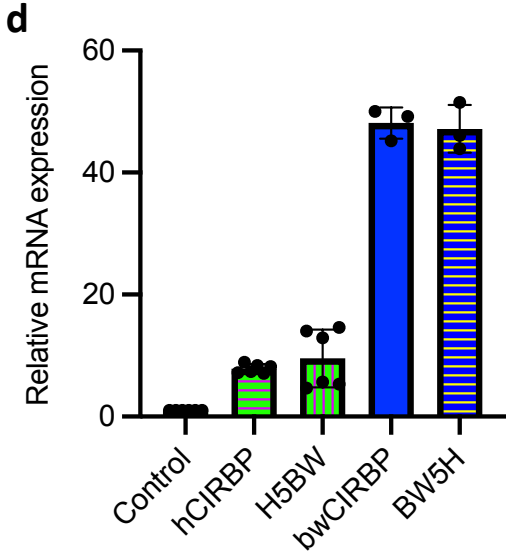
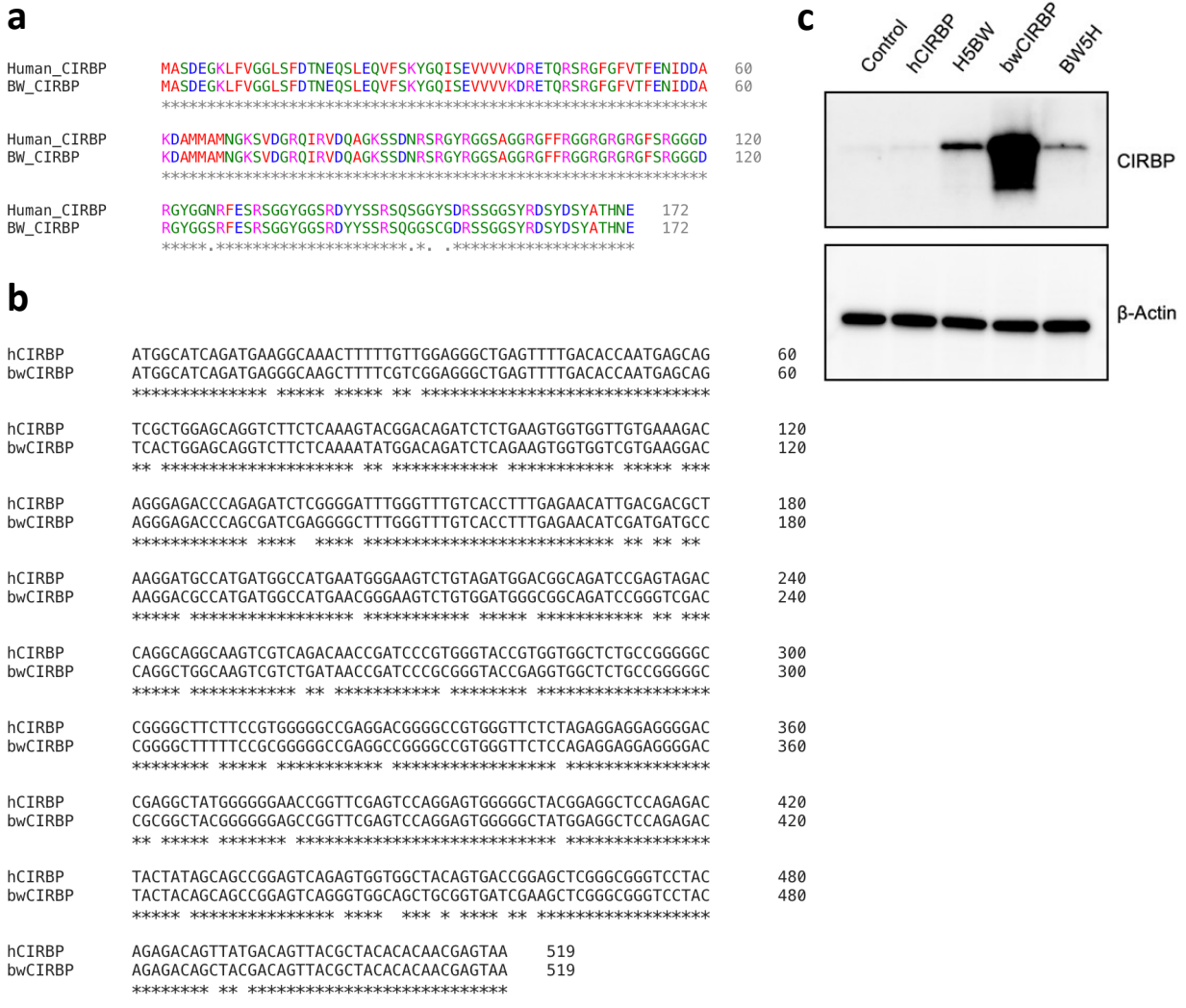
**Extended Data Figure 6. CRISPR indel size percentiles.** **a**, Indel size at the specified percentile rank (left column) by cell line and species, based on frequency of each indel size in sequencing data, ranked from most negative (largest deletions) to most positive (largest insertions), with unmodified or substitution-only alleles excluded. **b**, Pearson correlation between 5<sup>th</sup> percentile indel size and species lifespan ( $r=0.8508$ , 95% CI = 0.5125 to 0.9605,  $p=0.0009$ ,  $n=11$ ).



**Extended Data Figure 7. Proteomic and transcriptomic quantification of DNA repair proteins.** **a**, Heatmap of LC-MS protein abundance for primary fibroblasts of the indicated species and proteins. Color scale corresponds to  $\log_{10}$  ion intensity. **b**, Heatmap of transcript expression from RNA-seq of primary fibroblasts for the indicated species and transcripts. BW, bowhead whale; H, human. Numbers represent different cell lines. Color scale corresponds to normalized transcript abundance as described in Methods. **c**, Western blot of RPA2 in cultured skin fibroblasts, using 2 different monoclonal primary antibodies targeting conserved epitopes and normalized to histone H3. Each lane is a primary fibroblast line from a different adult individual. Fluorescent secondary antibodies were used to increase linear dynamic range for higher quantitative accuracy. **d**, Western blot for CIRBP with 3 different antibodies in 3 fibroblast lines per species. mAb, monoclonal antibody; pAb, polyclonal antibody.



**Extended Data Figure 8. Bowhead whale CIRBP stimulates NHEJ in MEFs and effect of temperature on CIRBP expression.** **a**, Effect of bwCIRBP expression on NHEJ in MEFs. CIRBP was expressed in mouse embryonic fibroblasts containing chromosomally integrated NHEJ reporter cassettes. (N=3). MEF, mouse embryonic fibroblasts. **b**, Western blot of CIRBP in human and bowhead whale primary skin fibroblasts at different temperatures. **c**, Relative endogenous CIRBP mRNA expression by qRT-PCR in 3 different human and 3 different bowhead whale cell lines. Error bars represent mean  $\pm$  SD. \*\* p<0.01. \*\*\* p<0.001 (two-tailed t-test).



CDS variant	CAI
hCIRBP	0.811
bwCIRBP	0.845
H5BW	0.809
BW5H	0.848

**Extended Data Figure 9. Effect of CIRBP mutations on mRNA and protein expression.** **a**, Human and whale CIRBP differ by only 5 amino acids. Alignment of bowhead whale and human CIRBP amino acid sequences (Clustal Omega). **b**, Alignment of bowhead whale and human CIRBP coding sequences (Clustal Omega). **c**, Western blot of bwCIRBP, hCIRBP, and reciprocal amino acid mutants overexpressed in human cells. **d**, Total CIRBP mRNA levels in human cells analyzed by qRT-PCR 24h after transfection of plasmids containing either wild type (hCIRBP, bwCIRBP) or mutants encoding hCIRBP with 5 amino acids mutated to whale sequence (H5BW) or bwCIRBP with 5 amino acids from human sequence (BW5H).  $\beta$ -Actin was used for data normalization. Units shown on the graph are relative to human basal endogenous CIRBP mRNA abundance (n=3). **e**, Calculated codon adaptation index (CAI)<sup>53</sup> for CIRBP coding sequence variants. Error bars are mean  $\pm$  SD.